Nanoscale

Accepted Manuscript

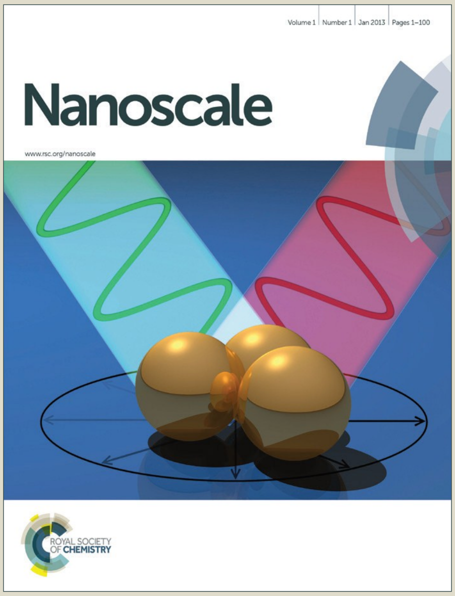

ROYAL SOCIETY OF CHEMISTRY

www.rsc.org/nanoscale

2D Nanosheet Molybdenum Disulphide (MoS_2) Modified Electrodes Explored Towards the Hydrogen Evolution Reaction

Samuel J. Rowley-Neale[1], Dale A. C. Brownson[1], Graham C. Smith[2], David A. G. Sawtell[1],
Peter J. Kelly[1] and Craig E. Banks[1]*

[1]: *Faculty of Science and Engineering, School of Science and the Environment,*
Division of Chemistry and Environmental Science, Manchester Metropolitan University,
Chester Street, Manchester M1 5GD, UK.

[2]: *Faculty of Science and Engineering, Department of Natural Sciences, University of*
Chester, Thornton Science Park, Pool Lane, Ince, Chester CH2 4NU, UK.

*To whom correspondence should be addressed.
Email: c.banks@mmu.ac.uk; Tel: ++(0)1612471196; Fax: ++(0)1612476831
Website: www.craigbanksresearch.com

Abstract

We explore the use of two-dimensional (2D) MoS_2 nanosheets as an electrocatalyst for the Hydrogen Evolution Reaction (HER). Using four commonly employed commercially available carbon based electrode support materials, namely edge plane pyrolytic graphite (EPPG), glassy carbon (GC), boron-doped diamond (BDD) and screen-printed graphite electrodes (SPE), we critically evaluate the reported electrocatalytic performance of unmodified and MoS_2 modified electrodes towards the HER. Surprisingly, current literature focuses almost exclusively on the use of GC as an underling support electrode upon which HER materials are immobilised.

2D MoS_2 nanosheet modified electrodes are found to exhibit a coverage dependant electrocatalytic effect towards the HER. Modification of the supporting electrode surface with an optimal mass of 2D MoS_2 nanosheets results in a lowering of the HER onset potential by *ca*. 0.33, 0.57, 0.29 and 0.31 V at EPPG, GC, SPE and BDD electrodes compared to their unmodified counterparts respectively. The lowering of the HER onset potential is associated with each supporting electrodes individual electron transfer kinetics/properties. The effect of MoS_2 coverage is also explored. We reveal that its ability to catalyse the HER is dependent on the mass deposited until a critical mass of 2D MoS_2 nanosheets is achieved, after which its electrocatalytic benefits and/or surface stability curtail. The active surface site density and turn over frequency for the 2D MoS_2 nanosheets is determined, characterised and found to be dependent on both the coverage of 2D MoS_2 nanosheets and the underlying/supporting substrate. This work is essential for those designing, fabricating and consequently electrochemically testing 2D nanosheet materials for the HER.

Keywords: Molybdenum disulphide (MoS_2); Hydrogen evolution reaction; Hydrogen economy; Carbon; 2D Electrochemistry; Sustainability.

1. Introduction

The increasing scarcity of fossil fuels coupled with the consequences of anthropogenic climate change has produced a global need to find feasible alternatives to energy generation.[1-3] One scenario of change is creating a global hydrogen economy in which energy generation demands are met partially or entirely by hydrogen fuel cells.[4-6] Utilising hydrogen fuels in this manner would cause a dramatic decrease in the anthropogenic greenhouse emissions and ozone precursors released by fossil fuel combustion given that the major product of hydrogen oxidation is H_2O.[4, 7] The main barrier to the implementation of such a hydrogen economy is, of course, the production of hydrogen. This requires an energy input that could feasibly be drawn from renewable energy sources such as wind, solar, and wave.[3, 8-10]

A common method of hydrogen production is the Hydrogen Evolution Reaction (HER) ($2H^+ + 2e^- \rightarrow H_2$), which involves the electrocatalytic splitting of water, known to occur *via* one of two routes; these being either the Volmer-Tafel or the Volmer-Heyrovsky reactions. [11,12, 13] The efficiency of the HER is dependent on the choice of electrocatalyst, with an optimal catalyst having a binding energy for adsorbed H^+ close to that of the reactant or product.[7] Currently, the most proficient catalyst for the HER is platinum (Pt) which has a small binding energy for the reaction to occur, resulting in the reaction proceeding at a near zero over-potential.[7, 11, 14, 15] Pt is a precious metal with a low natural abundance of 0.001–0.005 mg kg^{-1}within the Earth's crust. This coupled with its high demand result in Pt having a very high cost.[16] Consequently, current research is focused on finding a cheaper, more sustainable catalyst for the HER whilst maintaining performance and offering a binding energy towards H^+ close to that of Pt,[7] thus making a hydrogen based energy economy substantially more feasible.

Carbon based materials have long been utilised as electrodes in a plethora of analytical and industrial electrochemical applications.[17-23] They have the distinct advantage of being comparatively cheap and easily obtainable compared to the traditional noble metal based electrodes, particularly out-performing said metals in numerous significant areas due to carbon's structural polymorphism, chemical stability, wide operable potential windows and relative inert electrochemistry.[17, 18] Carbon based electrodes are often used as the supporting material for a plethora of electrocatalytic materials which lower HER onset potentials and thus greatly improve the HER kinetics in comparison to the bare/unmodified carbon based electrode.[1, 7, 24-28]

One example of where modified electrodes have been utilised to improve the HER has been reported by Liu, *et al.* [29] who utilised carbon nanotubes decorated with CoP nanocrystals deposited onto GC electrodes with a coverage of 0.285 mg cm^{-2} which resulted in the onset potential for the HER to reduce by to –40 mV. Other prominent examples from the literature have used graphene as electrocatalyst supports.[24, 27, 30, 31] The current challenge within HER research is finding a low-cost, abundantly available, non-polluting catalyst which is capable of matching the HER onset potential observed when Pt is used as a catalyst. Towards this goal, Mo based catalysts have been explored towards the HER. Table 1 presents a through literature overview of Mo based electrocatalysts explored towards the HER which is a combination and adaptation of work presented in papers by Joesen, Li and Ji [32-34] in addition to recent literature reports. It is evident that MoS_2 and $MoSe_2$ have shown promising results as HER catalysts. MoS_2 is a semiconductor with a direct band gap of *ca.* 1.9 eV and excellent charge carrier mobility (reported to be no less than 200 cm^2 V^{-1} S^{-1}).[35] It has been beneficially implemented in numerous electrochemical applications, such as in transistors, sensors, solar cells, and lithium ion batteries.[1, 36, 37]

Researchers have directed attention towards 2D MoS_2 where a single layer comprises of two monoatomic planes of hexagonally arranged sulphur atoms linked to molybdenum atoms[7, 38] and have been reported to be electrocatalytic towards the HER. [26, 27, 34, 38] For example, MoS_2 has been reported to exhibit electrocatalytic behaviour, attributed to it having a Density Function Theory (DFT) calculated binding energy towards H^+ of +0.08 eV at its edge.[7] Such catalytic activity was however, shown to be anisotropic, with the basal plane of the MoS_2 nanosheet being relatively inert and the exposed sulphur edges being the active sites of electron transfer.[7, 13, 26, 33, 39, 40] Resultantly, highly defected sheets of MoS_2 have a greater catalytic activity due to the larger number of exposed edges.[14] The MoS_2 edge-terminated sites have high energy kinetics, [26] thus making their production difficult as thermodynamic instability results in the active edges forming fullerene-like structures, which have few exposed edge sites.[26] In its 'bulk' form, MoS_2 is an inefficient HER catalyst due to it possessing a low ratio of exposed electroactive edges to inert basal-like planes and a high resistance resulting in slow ion transfer.[1, 34, 41] Interestingly, 2D MoS_2 nanosheets have been reported to possess 13× more active sites compared to the alternative bulk MoS_2. [42,50]

The current literature (see Table 1) glassy carbon (GC) has been exclusively used as a supporting electrode material, with few attempts to use alternative carbon based supports; this is clearly evident from inspection of Table 1.[21, 34, 43-45] For instance, Voiry, *et al.* [43] reported a low HER onset potential of *ca*. 100 mV for the HER using typical MoS_2 nanosheets deposited on a GC electrode. Yu, *et al.* [46] demonstrated a layer dependent electrocatalysis using MoS_2 (grown *via* chemical vapour disposition (CVD)) deposited on GC which is correlated with electron hopping in the vertical direction of the MoS_2 layers. Other work utilising modified GC electrodes has demonstrated that edge exposed MoS_2 nanosheets are efficient HER catalysts and that bulk MoS_2 has low activity.[42, 47] This work indicates that an MoS_2 structure with a greater proportion of MoS_2 edge sites to basal planes will likely give rise to improved HER kinetics, with an optimal material having a small geometric basal plane contribution (which is reportedly less active to the HER).[42] It has been shown that electrocatalytic activity towards the HER correlates linearly with the number of MoS_2 edge sites.[14]

The above studies are elegant in their approaches towards HER; however, they are lacking significantly from not altering the underlying electrode material and in doing so neglecting the ability to de-convolute the true electrochemical performance of 2D MoS_2 nanosheets. It is also important to realise that a cheap electrode support will be required in the application of electrocatalysts utilised in the HER. Graphite screen-printed electrodes (SPEs) meet this criteria due their advantages over other carbon based electrodes which include scales of economy resulting in ultra-low cost of production, competitive electron transfer performance/properties, versatility, and the ability to tailor and mass-produce such electrodes.[48] Note that the performance of MoS_2 can only be truly understood *via* immobilisation using a range of support materials with varying electrode kinetics (electrochemical activities). Such control experiments are explored herein which are usually overlooked in the current literature. Secondly, it is usual practise within the literature to modify electrodes with only one mass (coverage) of MoS_2, which again makes it difficult to extrapolate a true understanding of 2D MoS_2 nanosheets electrochemical behaviour; again this critical parameter is explored in this paper.

Inspired by the above insights and attempts in the literature to utilise MoS_2 as an alternative catalyst to Pt for the HER, this paper explores the use of 2D MoS_2 nanosheet modified carbon based electrodes towards the possible electrocatalysis of the HER. The 2D MoS_2 nanosheets are thoroughly characterised with scanning electron microscopy (SEM), transmission electron Microscopy (TEM), Raman spectroscopy, energy dispersive spectroscopy (EDS), X-ray diffraction (XRD), UV-visual spectroscopy and X-ray photoelectron spectroscopy (XPS). Linear sweep voltammetry is utilised to measure the onset of the HER with four carbon based electrodes as the underlying support materials, namely edge plane pyrolytic graphite (EPPG), glassy carbon (GC), boron-doped diamond (BDD) and screen-printed graphite electrodes (SPE). This work is distinct from the literature given that we explore a range of electrodes substrates, correlate our electrochemical responses with supplementary Raman mapping of the electrode surface (and other complementary physicochemical characterisation) and explore the effect of MoS_2 coverage; each noted component is routinely overlooked in the literature. We also benchmark the electrochemical performance of the 2D MoS_2 nanosheets towards the HER (utilising turn over frequency (ToF) calculations) and compare our results to Pt and literature reports.

2. Experimental section

All chemicals used were of analytical grade and were used as received from Sigma-Aldrich without any further purification. All solutions were prepared with deionised water of resistivity not less than 18.2 MΩ cm and were vigorously degassed prior to electrochemical measurements with high purity, oxygen free nitrogen. The above ensures the removal of any trace of oxygen from test solutions, which if present would convolute the observed results for HER with the competing oxygen evolution reaction (OER); this is common practice in the literature. [49, 50] All measurements were performed in 0.5 M H_2SO_4.

Electrochemical measurements were performed using an Ivium Compactstat ™ (Netherlands) potentiostat. Measurements were carried out using a typical three electrode system with a Pt wire counter and a saturated calomel electrode (SCE) reference electrode. The working electrodes used were as follows: an edge plane pyrolytic graphite (EPPG) (Le Carbone, Ltd. Sussex, UK) electrode, which was machined into a 4.9 mm diameter, with the disc face parallel with the edge plane as required from a slab of highly ordered pyrolytic graphite (HOPG, highest grade available with a lateral grain size, L_a of 1–10 µm and 0.4 ± 0.1° mosaic spread); a glassy carbon (GC) electrode (3 mm diameter, BAS, USA); a boron-doped diamond (BDD) electrode (3 mm diameter, BAS, USA); a Pt electrode (3 mm diameter, BAS, USA); and screen-printed graphite electrodes (SPE), which have a 3 mm diameter working electrode. The SPEs were fabricated in-house with appropriate stencil designs using a DEK 248 screen-printing machine (DEK, Weymouth, U.K.). For their fabrication first, a carbon-graphite ink formulation (product code C2000802P2; Gwent Electronic Materials Ltd., U.K.) was screen-printed onto a polyester (Autostat, 250 µm thickness) flexible film (denoted throughout as standard-SPE); these electrodes have been used extensively in other work.[48, 51-53] This layer was cured in a fan oven at 60 °C for 30 minutes. Next, a silver/silver chloride reference electrode was included by screen-printing Ag/AgCl paste (product code C2040308D2; Gwent Electronic Materials Ltd., U.K.) onto the polyester substrates. Finally, a dielectric paste (product code D2070423D5; Gwent Electronic Materials Ltd., U.K.) was then printed onto the polyester substrate to cover the connections. After curing at 60 °C for 30 minutes the SPEs are ready to be used. SPEs have been reported previously and shown to exhibit a heterogeneous electron transfer rate constant, k^o, of *ca*. 10^{-3} cm s^{-1}, as measured using the $[Ru(NH_3)_6]^{3+/2+}$ redox probe.[48, 54-57] Note that for the purpose of this work, electrochemical experiments were performed using the working electrode of the SPEs only and that external reference and counter electrodes were utilised as detailed earlier to allow a direct comparison between all the utilised electrodes.

The 2D MoS_2 nanosheets were commercially procured from 'Graphene Supermarket' (Reading, MA, USA).[58] The 2D MoS_2 nanosheets have a reported purity of >99 % and are dispersed in ethanol at a concentration of 18 mg L^{-1}.[58] The suspended flakes are reported to have an average lateral flake size of 100–400 nm and a thickness of between 1 and 8 monolayers.[58] The modification of each electrode was carried out using a drop casting approach, where an aliquot of the 2D MoS_2 nanosheet suspension was deposited onto the desired supporting electrode surface using a micropipette.[54] This deposition was then allowed 5 minutes to dry (at 35 ^{o}C) to ensure complete ethanol evaporation. Finally, the electrode was allowed to cool to ambient temperature, after which the process was repeated until the desired mass was deposited onto the surface. The electrode was then ready to use.

An Agilent 8453 UV-visible Spectroscopy System (equipped with a tungsten lamp assembly, G1315A, 8453 for absorption between 250 nm and 1500 nm and a deuterium lamp, 2140-0605 for absorption between 200 nm and 400 nm) was used to obtain the absorption spectroscopy. The absorption spectra was analysed using the UV-Visible ChemStation software. Scanning electron microscope (SEM) images and surface element analysis were obtained using a JEOL JSM-5600LV model SEM equipped with an energy-dispersive X-ray microanalysis (EDS) package. Raman Spectroscopy was next performed using a 'Renishaw InVia' spectrometer equipped with a confocal microscope (×50 objective) and an argon laser (514.3 nm excitation). Measurements were performed at a very low laser power level (0.8 mW) to avoid any heating effects. XRD was performed using an "X'pert powder PANalytical model" with a copper source of K_α radiation (of 1.54 Å) and K_β radiation (of 1.39 Å), using a thin sheet of nickel with an absorption edge of 1.49 Å to absorb K_β radiation. The Omega was set to 3.00 and the 2θ range was set between 10 and 100 2θ in correspondence with literature.[32] Additionally, to ensure well defined peaks an exposure of 100 seconds per 2θ step was implemented. 2D MoS_2 nanosheets were utilised after deposition onto a sterilised glass slide (coated with excess 2D MoS_2 nanosheets in ethanol then allowed to dry). The XPS data was acquired using a bespoke ultra-high vacuum system fitted with a Specs GmbH Focus 500 monochromated Al Kα X-ray source, Specs GmbH Phoibos 150 mm mean radius hemispherical analyser with 9-channeltron detection, and a Specs GmbH FG20 charge neutralising electron gun.[59] Survey spectra were acquired over the binding energy range 1100 – 0 eV using a pass energy of 50 eV and high resolution scans were made over the C 1s and O 1s lines using a pass energy of 20 eV. Under these conditions the full width at half maximum of the Ag $3d_{5/2}$ reference line is ~0.7 eV. In each case, the analysis was an area-average over a region approximately 1.4 mm in diameter on the sample surface, using the 7 mm diameter aperture and lens magnification of ×5. The energy scale of the instrument is calibrated according to ISO 15472, and the intensity scale is calibrated using an in-house method traceable to the UK National Physical Laboratory.[60] Data were quantified using Scofield cross sections corrected for the energy dependencies of the electron attenuation lengths and the instrument transmission.[61] Data interpretation was carried out using CasaXPS software v2.3.16.[62]

3. Results and Discussion

3.1 Characterisation of 2D MoS_2 nanosheets

3.1.1 UV-VIS and lateral grain size calculations

The lateral length (L_a) and number of the commercially procured 2D MoS_2 nanosheets can be readily deduced from absorption spectroscopy. It has been observed that actually the terminology is more correctly optical extinction spectroscopy since the optical beam interacts with the dispersed nanosheets by both absorption and scattering.[63-65] The extinction coefficient of dispersed 2D MoS_2 nanosheets is 6,820 L g^{-1} m^{-1}at the local minimum of 345 nm, using this information along with a spectra it is possible to determine the concentration of dispersed 2D MoS_2 nanosheets. [64] Varrla, *et al.* [63] uses this information to calculate the concentration as a function of mixing parameters whilst also showing that the extinction spectra can be used to determine information regarding the 2D MoS_2 nanosheet length and thickness. ESI Figure 1 shows the optical extinction spectra of the commercially procured MoS_2 nanosheets which are dispersed in ethanol. It is readily evident that the spectra displays A- and B- excitonic transitions as well as other pertinent features consistent with the 2H polytype of MoS_2 and is consistent with MoS_2 nanosheets produced *via* shear exfoliation.[63, 64, 66] The extinction spectrum of the 2D MoS_2 nanosheets allows one to readily determine the mean nanosheet lateral length due to the effect 2D MoS_2 nanosheet edges upon the spectral profile. The extinction spectrum also allows the number of layers (thickness) to be determined as a result of quantum confinement effects causing a well-defined shift A-exciton position corresponding to nanosheet thickness .[64] The lateral length, $L(\mu m)$ of the MoS_2 can be deduced from the following equation:

$$L(\mu m) = \frac{3.5\left(Ext_B / Ext_{345}\right) - 0.14}{11.5 - \left(Ext_B / Ext_{345}\right)} \qquad [1]$$

where $\left(Ext_B / Ext_{345}\right)$ is the ratio of extinction at the B-excition to that at 345 nm since the spectral profile is dependent upon the lateral length of the MoS_2. Further information can be obtained in terms of the number of nanosheets, N_{MoS_2} expressed as the number of monolayers per nanosheet can be determined from the wavelength associated with the A-excition, since the quantum conferment effects result in well-defined shifts in the A-excition position with the thickness of the nanosheet; this is summarized by the following equation:

$$N_{MoS_2} = 2.3x10^{36} e^{-54888/\lambda_A} \quad [2]$$

From the spectra presented in ESI Figure. 1 the lateral length and number of MoS_2 nanosheets are determined to correspond to 61.5 nm and 3 (2.89) respectively. We note that the lateral size is smaller than the value given by the commercial supplier. The average of 3 monosheets per nanosheets agrees strongly with the commercial supplier who notes the number of monolayers per nanosheet to be between 1-8 in solution.[58] It is important to point out that the lateral size and the number of MoS_2 sheets are for when these are in solution; when immobilised upon a surface these will deviate from these measured values, as we will see later, but is a common issue in the whole of the literature.

3.1.2 SEM, TEM, Raman, EDS and XRD

Independent physicochemical characterisation of the 2D MoS_2 nanosheets was performed. SEM and TEM images of the commercially sourced 2D MoS_2 nanosheets are shown in ESI Figures. 2 and 3. Despite some aggregation, which is the case for all nanosheet materials, upon close inspection, their appearance is within the acceptable widths with a lateral size of *ca* 100-400 nm evident as quoted by the supplier and measurements undertaken above. The 2D MoS_2 nanosheets immobilised upon the silicon wafer generally exhibit a uniform coverage. Complimentarily EDS mapping analysis was performed to offer insight into the elemental composition of the area shown in ESI Figure 2. Analysis of the EDS map shows uniform distribution of Mo and S atoms with a ratio of 0.55% At. and 1.35% At. and this composition correlates with expected values for the structure of 2D MoS_2 nanosheets (*ca*. 1:2 ratio of Mo and S respectively) agreeing with independent literature.[35] Additionally, XRD analysis showed a characteristic (002) diffreaction peaks for the MoS_2 nanosheets with 2θ corresponding to 14.2^0 indicating the presence of MoS_2 via the reflection of separated MoS_2 layers, see ESI Figure. 4 which is in agreement with literature reports.[32, 41] The peak at 28 2θ is attributed to the supporting glass slide. Last, the Raman spectra for the 2D MoS_2 nanosheets after deposition on a serialised silicon disk are presented in Figure 1. The characteristic peaks associated with MoS_2 at *ca*. 380 and 405 cm^{-1} are clearly evident, corresponding to that reported in the literature.[67] Further analysis is described later where Raman mapping is utilised to explore MoS_2 mass modifications deposited onto electrode surface.

3.1.3 *XPS*

MoS_2 nanosheets suspended in ethanol were prepared for X-ray photoelectron spectroscopy (XPS) analysis by pipetting a few drops of the suspension onto a fragment of a clean Si (111) wafer and allowing the ethanol to evaporate. The XPS spectrum is shown in ESI Figure 5 and the results of the surface composition analysis (excluding hydrogen) are shown in ESI Table 1. The C and O present is likely a result of residuals from the ethanol used to disperse the MoS_2. This is supported by the presence of a component peak at *ca*. 286.6 eV showing that alcohol groups were present on the sample surface. The Si present can be accounted for by the use of a Si (111) wafer as an underlying support material for the drop coating. Na is likely present from an organic Na contaminant or *via* contributions from the supporting wafer. The Mo to S % atomic concentrations are observed at a 1:2.2 ratio respectively, agreeing well with the Raman and EDS analysis performed above (further indicating the presence of the target material). Shin, *et al.* [68] theorises the deviation from an expected stoichiometry ratio of 1:2 for Mo and S respectively in 2D MoS_2 nanosheets is due to the presence of MoS_3.[63] It is of note that Mo is present in three valence states, with each of the valence states consisting of a Mo $3d_{5/2}$ and Mo $3d_{3/2}$ doublet. The curve-fitted high resolution Mo 3d spectral region is shown in ESI Figure 6. The area ratios of the doublets are constrained to the ratios of the Scofield cross sections (*i.e.* Mo $3d_{3/2}$ = 0.6904 x Mo $3d_{5/2}$), the two components of each doublet are constrained to the same line shape and ‘full width at half maximum’, and their separations are fixed at the known reference value of 3.13 eV. The $3d_{5/2}$ components were found at 229.4 eV (Mo^{4+}), 231.6 eV (Mo^{5+}) and 233.1 eV (Mo^{6+}). The spectral region also includes the S 2s peak at 226.6 eV.

3.2 Electrochemical activity at assigned coverage

The electrochemical response of the 2D MoS_2 nanosheets (1266.7 ng cm^{-2}) immobilised upon SPEs were studied using cyclic voltammetry (CV). Figure. 2 shows a typically observed CV where two oxidation peaks at + 0.65 and + 1.0 V are clearly visible in the first cycle followed by several minor reduction peaks in the – 0.5 to – 1.5 V range. The initiation of the HER is evident in the cathodic response, with an onset potential of *ca* 1.1 V. In terms of the anodic response, the two prominent oxidation peaks are due to irreversible reactions, likely the oxidation of Mo^{4+} to Mo^{6+} at edge and basal sites. Such oxidations are not observable in subsequent scans, which is likely due to the MoO_3 dissolving into solution or being reduced to Mo^{3+}, at which point it dissolves, explaining the origin of the observed reduction peak. This is represented in the equation below. [69]

$$MoS_2 + 7H_2O \rightarrow MoO_3 + SO_4^{2-} + ½S_2^{2-} + 14\ H^+ + 11e^- \qquad [3]$$

It may also be possible that the Mo within our 2D MoS_2 nanosheets has two dominant valence states, both of which are oxidised, resulting in the presence the double peak. This inference is supported by the independent XPS analysis (see earlier), which indicated the presence of Mo in three different valance states for the 2D MoS_2 nanosheet sample analysed. The double oxidation peak observed in Figure. 2 is of interest and further study is required to determine its exact cause. The observed voltammetry (see Figure 2) is in good agreement with Bonde, *et al.* [69] who explored nano-MoS_2, deposited onto toray carbon paper in 0.5 M H_2SO_4, towards the HER. If the potential window is kept below the range where reported oxidation peaks occur, the HER activity of nano-MoS_2 remains stable.[70] The reduction peaks can also be accounted for by the reduction of S_2^{2-} to H_2S.[69] The double oxidation peak has previously been mischaracterised as a single oxidation peak due to the peaks merging occurring as a result of performing cyclic voltammetry at too high a scan rate.[71] This is important to note as the double peak convolutes the understanding of the electrochemical process occurring.

Next, attention was turned to benchmarking our electrochemical system for the HER using commonly available electrodes in 0.5 M H_2SO_4, as is widespread practise within the literature.[14, 69, 72] As is evident in Figure. 3(A), the four unmodified carbon based electrodes are all significantly inferior to a Pt electrode with respect to the potential required for HER onset and the current density reached. Note that the onset of HER is analysed as the potential at which the observed current initially begins to deviate from background current. This is to be expected with Pt being a pure metal which has a very small binding energy for H^+.[7] It is evident that the onset potential for the HER occurs at *ca*. –1.05, –0.78, –0.76 –0.73, and –0.25 V at the GC, EPPG, BDD, SPE, and Pt electrodes respectively. The SPEs exhibit the lowest onset potential for the HER when compared to all of the carbon-based electrodes utilised herein. The bare GC electrode exhibited the largest HER onset potential, indicating that it is not a beneficial electrode for the HER.

It is of note that the current density obtained at each of the unmodified electrodes towards the HER and how this progressively alters during the course of the measurement. Although it is apparent that a higher potential is required to initiate the HER at the GC electrode (by *ca.* –0.3 V in contrast to the alternative carbon based electrodes), the current density recorded at this electrode appears to surpass that of the alternative materials.

3.2.1 Tafel analysis

A common approach in the literature is to employ Tafel analysis allowing the most likely electrochemical process to be theorised. Literature has suggested three possible steps in the reaction, each of which is capable of being the rate-determining step of the HER; this analysis is dependent on the corresponding Tafel slope. The initial H^+ discharge step being the Volmer reaction, leading to the following equation:[11-13]

H_3O^+ (aq) + e^- + catalyst → H (ads) + H_2O (l) [4]

$$\frac{2.303RT}{\propto F} \approx 120mV$$

The Volmer step can then be followed by one of two possible steps; either the Heyrovsky step:

H (ads) + H_3O^+ (aq) + e^- → H_2 (g) + H_2O (l) [5]

$$\frac{2.303RT}{(1+2)F} \approx 40mV$$

or the Tafel step:

H (ads) + H (ads) → H_2 (g) [6]

$$\frac{2.303RT}{2F} \approx 30mV$$

where the transfer coefficient (α) is 0.5, F is the Faraday constant, R is the universal gas constant and T is the temperature at which the electrochemical experiment was performed at. The values from the Tafel analysis (presented below each equation) are an indication of the reaction mechanism. Tafel analysis was performed on the Faradaic sections of the LSV plots which can be observed in Figure. 3(A). Tafel analysis was performed on the data presented in Figure. 3(A) where the corresponding analysis is presented in Figure. 3(B), which yielded Tafel values of *ca.* 89.2, 64.4, 94.4 and 81.2 mV dec^{-1} for the unmodified EPPG, GC, SPE and BDD electrodes respectively. Using the above values for the unmodified electrodes, interpretation of the Tafel slopes reveals that the adsorption Volmer step is likely rate limiting for the SPE and EPPG electrodes. The discharge Heyrovsky step is most likely the rate limiting step at the GC electrode.[11-13] In the case of BDD, Tafel analysis does not allow a definitive mechanism to be estimated.

We next explore the use of 2D MoS_2 nanosheet modified carbon based electrodes towards the HER. As detailed in the introduction, the aim of this paper is to tackle the current issue of finding a cheap, more abundant, electrocatalyst alternative to Pt for the HER.[7, 11] We investigate the potential current state of the art (2D MoS_2 nanosheets) and compare this to our benchmarking experiments with the aim of revealing valuable insights. First, the range of carbon based electrodes utilised above (namely GC, BDD, EPPG and SPEs) are modified with different masses of the 2D MoS_2 nanosheets. Note that using various underlying support materials is seldom seen in the current literature and thus it is important that such control experiments are explored and reported herein for the first time. Inspection of Figure. 4(A) reveals that using a 1267 ng cm^{-2} modification of 2D MoS_2 nanosheets results in a lowering of the potential required for onset of the HER and is accompanied by an increase in the observed current density, signifying an improved electrochemical response at each of the underlying electrode substrates utilised. Specifically, the HER onset potential was lowered to *ca.* –0.45, –0.48, –0.44 and –0.45 V for EPPG, GC, SPE, and BDD electrodes respectively. Clearly, these newly obtained values are significantly closer to the reported value using a Pt electrode (*ca.* –0.25 V) than the initial values reported above at the unmodified carbon based electrodes. This implies that the 2D MoS_2

nanosheets are effective electrocatalysts for the HER.

Tafel analysis was performed on the modified LSV profiles. Tafel slope values of *ca.* 74.7, 41.4, 90.0, and 90.9 mV dec^{-1} were estimated at the EPPG, GC, SPE and BDD electrodes respectively (shown in Figure. 4(B)). Comparison of the Tafel values suggests that modification of the support electrodes with 2D MoS_2 nanosheets does not cause a significant alteration in the mechanism or indeed the Faradic current density of the HER.[42] This however, is not the case when utilising the GC electrode, which exhibited a reasonable increase in current density resulting in the 'discharge Heyrovsky' step more likely becoming the rate limiting step. This implies that modification with the 2D MoS_2 nanosheets allows for increased and sufficient H^+ adsorption, thus in turn catalysing the HER process.

In terms of analysing the current densities obtained, deposition of the 2D MoS_2 nanosheets at a coverage of 1266.7 ng cm^{-2} induces higher exchange current densities when compared to the unmodified alternative. It is likely that this results from the early onset of the HER (*i.e.* the decreased over-potential) and is not directly due to an overall increased reaction rate at the modified SPE and BDD electrodes given that comparison is based on analysis at specific potentials. For the GC and EPPG electrodes there was an increase in the current density, which is due not only the earlier HER onset potential but also an increased current density slope. This is likely a result of the structure of MoS_2 on these electrodes having a high number of exposed active edge sites allowing for a greater amount of H^+ adsorption.

3.3 Electrochemical activity at differing 2D MoS_2 nanosheet coverages

3.3.1 Raman analysis

The experimental data discussed above considers the use of 1267 ng cm^{-2} (2D MoS_2 nanosheet) modified electrodes. Currently it is common practice in the literature to choose only one mass of MoS_2 coverage when exploring its electrochemical performance (in addition to exploring this on only one underlying electrode surface, typically GC). As highlighted in the introduction, this practice results in convoluted interpretations of the performance of 2D MoS_2 nanosheets and thus diligent controls are required in order to reveal the true electrochemical response. We next consider this parameter and explore the effects of different mass coverages of 2D MoS_2 nanosheets on a given electrode.

In order to ascertain the level of MoS_2 coverage and relate this to the observed voltammetry, we first investigate the respective Raman properties of our modified electrodes. Figure. 5 depicts the effect that larger deposition quantities of MoS_2 onto a SPE has upon the recorded Raman Spectroscopy, where the evolution of the two characteristic peaks is evident and is discussed in more detail below. We first analyse the effect of coverage on the electrode surface using Raman mapping and a SPE as the underlying support material (as a representative model). Through comparison of the underlying graphite peak area at *ca.* 1550 cm^{-1} against the area of the MoS_2 Raman peaks at *ca*. 380 and 405 cm^{-1}, the surface area coverage of the electrode was investigated. It is evident that increasing the mass deposition of MoS_2 on the SPE surface results in an increased intensity in the respective assigned Raman peaks (see Figure. 5(A)). Raman maps are presented in Figure. 6 which concur with the previous inference and show that with increased mass deposition a thicker (largely uniform) layered coverage is achieved across the entire electrode surface. Through analysis of the respective Raman maps depicted in Figures. 6 and 7, it is likely that the deposition of 504 ng cm^{-2} 2D MoS_2 nanosheets results in the complete coverage of the underlying SPE support material (which has a surface area of 0.0707 cm^2). With each additional modification this layer of deposited MoS_2 will thicken (see Figure. 7). It is possible to determine the stacking number by comparison of E^1_{2g} and A_{1g} vibrational bands (VB) as the observed Raman spectrum evolves with the number of layers present. The E^1_{2g} VB results (at *ca*. 382 cm^{-2}) due to the opposite vibration of two S atoms in respect to a Mo atom, whereas the A_{1g} peak (at *ca*. 407 cm^{-2}) represents the S atoms vibrating in opposite directions and out of plane.[67, 73] Literature suggests that as MoS_2 moves from single layer to bulk the E^1_{2g} VB downshifts from 384 to 382 cm^{-2}, whilst A_{1g} VB shifts upwards from 403 to 408 cm^{-1}, where a separation of *ca*. 19 cm^{-1} between the VBs is indicative of single layer MoS_2 and a value of *ca*. 25 cm^{-1} represents the bulk material.[73] [26, 40] In this work we observe an increase in the Raman shift of the E^1_{2g} VB with greater mass additions from *ca*. 377 to 380 cm^{-1},(see Figure. 5(A)), however the response observed herein may result from the specific morphology and stacking structures of our MoS_2 on the underlying support material given that previous studies have reported a similar shift relating to the E^1_{2g} band and attributed this to uniaxial strain or heterostructure stacking.[74] Interestingly, analysis of the A_{1g} peak corresponds to the predicted theorem for a transition from single-layer to multi-layer 2D MoS_2 nanosheets with an increasing Raman shift from *ca*. 402 to 405 cm^{-1}.[40, 67]

Furthermore, when considering the separation of the two VBs (given that this value is also indicative of the number of MoS_2 layers present) the shift in the difference of the VB positions between A_{1g} and E^1_{2g} gives a consistent value of 24.7 cm^{-1} with increasing coverages, indicating that +4 layers (*i.e.* bulk) MoS_2 is present at all four mass coverages utilised herein (see Figure. 5(B)). Consideration of the above factors in conjunction with our independent lateral grain size calculations (UV-VIS) indicates that the structural model of the 2D MoS_2 nanosheets utilised herein is likely that of re-assembly, with the few-layer nanosheets forming bulk MoS_2 upon deposition onto the electrode surface. Further work on whether the morphology of a SPEs surface causes uniaxial strain and/or heterostructure stacking of the 2D MoS_2 nanosheets would be of great interest. Note that confirmatory tests were performed in which the aliquots deposited above were immobilised onto an alternative silicon wafer support in order to overcome potential issues with the underlying surface. Such control experiments (data not shown) exhibited the same separation values as identified above (*ca.* 25.1 cm^{-1}) between the two VBs and thus confirms that our 2D MoS_2 nanosheets likely form bulk MoS_2 once deposited/immobilised onto a support surface. It is thus likely that further additions of our material result in the formation of thicker or rougher 'bulk' layers. We next explore the electrochemical implications of this, often overlooked in the literature.

3.3.2 Electrochemical HER: critical mass of 2D MoS_2 nanosheets

Returning to the analysis of the HER, the effects of different mass deposition on the different electrode surfaces was next explored. Using a fixed potential (–0.75 V) at which each electrode exhibits an observable current, the current densities relating to the HER were recorded. It is evident through inspection of Figure. 8 that a trend of increased current density (corresponding to increased 2D MoS_2 nanosheet coverage (ng cm^{-2})) is subsequently followed by a decrease in current density and/or plateauing effect. This is apparent upon modification of each of the four underlying electrode materials studied with our material of interest. Over the modification range tested, the maximum/optimal current density was found to correlate to a 2D MoS_2 nanosheet coverage of *ca.* 1014.4, 1266.7, 1266.7, 1266.7 ng cm^{-2} for the GC, EPPG, SPE and BDD electrodes respectively. Tafel analysis on these optimal mass modifications reveals values of *ca.* 40, 74, 92 and 90.9 mV dec^{-1}. GC and BDD when modified with the 2D MoS_2 nanosheets demonstrate a fast discharge mechanism, with H^+ adsorption no longer the rate-limiting step.[1] Through analysis of the values reported above and comparison to the values reported in section 3.2.1 it is clear that of the four electrodes modified, electrodes with slower kinetics (such as the GC and BDD) exhibit a favourable electrocatalytic effect when modified with 2D MoS_2 nanosheets towards the HER. Contrary to this, the EPPG, which possesses faster underlying rate kinetics, exhibited only a slight change towards an altered reaction mechanism and further in the case of the SPE there was no observable change.

3.4 Assessment of 2D MoS_2 Nanosheets Catalytic Activity

An array of approaches are employed to study the intrinsic catalytic activity of 2D MoS_2 nanosheets within the literature. In order to deduce how the observable catalytic activity alters with changes in the mass of 2D MoS_2 nanosheet modification we employ two commonly used techniques below: the assessment of catalytic turn over frequency (ToF) and the number of active sites present on the surface of the electrode.[47, 68]

3.4.1 Turn Over Frequency (ToF)

In order to evaluate how the intrinsic catalytic activity of the 2D MoS_2 nanosheets alters with varying modification on a 'per active site' basis, the ToF was deduced using a method reported previously by Benck, *et al.* [47] their deriviation is repeated here for clarity using values associated with the 252 ng cm^{-2} modified SPE.[47, 75] In this calculation is is assumed that the surface of the 2D MoS_2 nanosheets is atomically flat (altough the true modification will have a finite roughness).[47] Taking the sulphur to sulphur bond distance to be 3.15 Å which corresponds to an area of 4.296 $Å^2$/S atom [47, 76] which can be used to calculate the surface area occupied by each MoS_2:

$$4.296\,\frac{Å^2}{S\ atom} * \frac{2\ S\ atom}{1\ MoS_2} = 8.593\,\frac{Å^2}{MoS_2} \qquad [7]$$

Using the dervied area for a MoS_2 molecule (corresponding to the number of surface sites for a flat standard) it is possible to determine the number of MoS_2 molecules per cm^2 geometric area:

$$\frac{1\ MoS_2}{8.593\ Å^2} * \frac{10^{16} Å^2}{0.0707\ cm^2} = 1.646 * 10^{16}\,\frac{MoS_2}{cm^2} \qquad [8]$$

The number of electrochemically accessible surface sites can be determined from the following:

$$\frac{\#\ Surface\ Sites\ (Catalyst)}{cm^2\ geometric\ area} = \frac{\#\ Surface\ Sites\ (Flat\ Standard)}{cm^2\ geometric\ area} * R_F \qquad [9]$$

It is also essential to accurately determine the roughness factor (*R_F*) for each modified electrode surface which was performed using white light profilometry (WLP) (See ESI Figure. 7) as is common within the literature. The described WLP technique yielded R_F values which represent the entire surface area of the electrode rather than electroactive area (see later). In the case of the 252 ng cm^{-2} modified SPE, the number of surface sites cm^{-2} corresponds to 3.16×10^{16} surface sites / cm^2. The following allows the ToF on a per-site basis to be determined:

$$TOF\ per\ site = \frac{\#\ Total\ Hydrogen\ Turn\ Overs\ /\ cm^2\ geometric\ area}{\#\ Surface\ Sites\ (Catalyst)/\ cm^2\ geometric\ area} \qquad [10]$$

Taking the value of current density (mA cm^{-2}) at the potential of –0.75 V (at a 100 mVs^{-1} scan rate) and using the R_F calculated via WLP, per-site the ToF can be deduced from the following:

$$\left(j\,\frac{mA}{cm^2}\right)\left(\frac{1\ A}{1000mA}\right)\left(\frac{1\ C/s}{1\ A}\right)\left(\frac{1\ mol\ e^-}{96{,}485.3\ C}\right)\left(\frac{1\ mol\ H_2}{2\ mol\ e^-}\right)\left(\frac{6.02214*10^{23}}{1\ mol\ H_2}\right) = 2.59*10^{15}\ \frac{H_2/s}{cm^2}\,per\,\frac{mA}{cm^2} \qquad [11]$$

Using equation 12 and value derived from formula 11, it is possible to determine a value for the ToF:

$$\left(2.59*10^{15}\ \frac{H_2/s}{cm^2}\Big/\frac{mA}{cm^2}\right)\left(10\,\frac{mA}{cm^2}\right)\left(\frac{1\ cm^2}{3.16*10^{16}\ surface\ sites}\right) = 0.81\,\frac{H_2/s}{surface\ sites}$$

[12]

At the chosen potential (– 0.75 V) the current densities were found to correspond to 0.83, 1.16 and 1.17 mA cm^{-2} for SPEs (SPEs used as representative example of the carbon based electrodes utilised) modified with 252, 1009 and 2019 ng cm^{-2} of 2D MoS_2 nanosheets. The R_F values calculated *via* the WLP method (which provides the topography of the uppermost surface, see roughness factor calculation method 1 in the ESI) were found to correspond to 1.918, 1.934 and 1.924 respectively. Using these values the ToF values deduced from the above equations were found to correspond to 0.81, 1.14 and 1.15 $\frac{H_2/S}{\text{Surface Site}}$. The stability of the WLP R_F values across the range of modifications results in a relatively little variation of the ToF values obtained. Benck, *et al.* [47] suggest that the upper and lower possible ToF could be one order of magnitude greater or less than the given value. If the chosen potential is altered to – 1.5 V the current densities at this potential are found to 4.25, 4.43 and 4.33 mA cm^{-2} for the 252, 1009 and 2019 ng cm^{-2} 2D MoS_2 nanosheets modified SPEs respectively. Using the same technique and WLP R_F values above however replacing the current densities at –0.75 V for those at –1.5 V the ToF values are 0.59, 0.61 and 0.6 $\frac{H_2/S}{\text{Surface Site}}$ for the 252, 1009 and 2019 ng cm^{-2} 2D MoS$_2$ nanosheets modified SPEs respectively. Clearly, alerting the potential at which the current densities are recorded has a significant affect upon the ToF recorded.

In order to deduce R_F values which are representative of the *true* electroactive area of an electrode, a double layer capacitance technique can be employed (see roughness factor calculation method 2 in the ESI). Note that the double layer capacitance technique is preferential to the WLP technique as it describes the true electroactive surface area of the electrode including accessible pores and the thickness of multiple layers deposited whereas WLP is limited in that it bases its calculated value off only a scan of the topography of the uppermost surface in question; simply, the WLP only probes the outermost layer and cannot determine a relatively thick layer from a thin layer. The double layer capacitance technique for determining R_F is reported in the ESI.

Taking the current density values corresponding to a – 0.75 V potential and replacing the WLP R_F values for 1.0, 3.3 and 4.8 which are the R_F values calculated *via* double layer capacitance, for SPEs modified with 252, 1009 and 2019 ng cm^{-2} of 2D MoS$_2$ nanosheets, the ToF was to correspond to 1.58, 0.6 and 0.46 $\frac{H_2/S}{\text{Surface Site}}$. The values estimated for the ToF herein are in rough agreement with the range of ToF values Xie, *et al.*[77] states should be expected for various types of MoS$_2$ structures. It is evident that as a result of increasing the mass of 2D MoS$_2$ nanosheets deposited onto an SPE there is a resulting decrease in the ToF ($\frac{H_2/S}{\text{Surface Site}}$). This is possibly the result of larger masses of 2D MoS$_2$ nanosheets, once deposited, forming a MoS$_2$ structure whereby there is increased shielding of active edge sites by inactive basal planes. [42, 47] Again, if the current densities are altered to those corresponding to a – 1.5 V potential whilst using the same technique and double layer capacitance R_F values, above, the ToF values deduced are 1.14, 0.37 and 0.24 $\frac{H_2/S}{\text{Surface Site}}$ for the 252, 1009 and 2019 ng cm^{-2} 2D MoS$_2$ nanosheets modified SPEs respectively. Of note is the significant affect that altering the potential, at which the current densities are measured, has upon the determined ToF values. This ability to manipulate the ToF value deduced makes it essential for literature to create an industry standard for what potentials should be used when dealing with ToF calculations. This would allow for more ready comparison between different studies involving ToF.

As previously stated the double layer capacitance technique provides a true electrocatalyic surface area of the given electrode whereas the WLP technique provides a scan of topography of the uppermost surface. It can therefore be assumed that the R_F values deduced *via* double layer capacitance offer more accurate ToF values.

3.4.2 Number of Active Sites

Determining the number of active sites present on the surface of an electrode offers valuable insight into its catalytic properties. Shin and co-workers [68] have shown that it is possible to derive the number of 2D MoS_2 nanosheet active sites (*N*) present on the surface of the catalyst using the following equation:

$$N = R_F(N_A d/M_f)^{2/3} \qquad [13]$$

where N_A is Avogadros number, d is the film density (*ca.* 2.35 x10^{-4} g cm^{-3}, which was derived *via* the use of WLP to observe the step height, in this case 21.9 µm, between the bare electrode surface and a mass of 514 ng cm^{-2} 2D MoS2 nanosheets deposited), M_f is the formula weight of MoS_2, and R_F is the roughness factor, which in this case is defined as the ratio of the real surface area to the geometric area. The geometric area (and the electrochemically active area) of the electrode surface can vary significantly due to the surface roughness and porosity of the sample. In this case the R_F was derived using double layer capacitance as it is linearly proportional to catalytic surface area (see roughness factor calculation method 2 in the ESI).[78] The double layer capacitance values determined (*via* cyclic voltammetry, see ESI Figure. 8) are 8.7, 68, 218, 322 µF cm^{-2} for SPEs modified with 0, 252, 1009 and 2019 ng cm^{-2} 2D MoS_2 nanosheets respectively. As a benchmark the double layer capacitance value for amorphous MoS_2 is reported recorded to be 66.7 µF cm^{-2}. [46] R_F values for SPEs modified with 252, 1009 and 2019 ng cm^{-2} of 2D MoS_2 nanosheets were estimated to be *ca* 1.02, 3.26 and 4.83 respectively. The R_F values derived using double layer capacitance show an increment with greater masses of 2D MoS_2 nanosheet modification. R_F values for BDD, EPPG, GC and SPE post modification are presented in Table 2. The number of active sites per cm^{-2} are summarised in Table 2 where there is a (positive) linear correlation between number of active sites and mass of MoS_2 deposited. It can therefore be asserted that there is a physicochemical change within the structure of the 2D MoS_2 present upon the surface of the electrode, which leads to the exposure of less active sites per additional ng cm^{-2} modification after a certain 'critical mass' (this is also evident through inspection of Figure 8), or no further increase in the number of the active sites accessible to the solution. It is clear that the number of active sites (and related HER performance) increase (improve) with the addition of larger quantities of MoS_2 onto the underlying electrode surface up until the specified critical mass is achieved.

It is evident that the increased mass deposition of 2D MoS_2 nanosheets on a given electrode surface results in an improvement in the current passed in addition to a lowered HER onset potential (improved electrochemical response). As is apparent from the above discussion (and inspection of Figure 8) this increase in the catalytic performance a given modified electrode material (which corresponds to the addition of 2D MoS_2 nanosheets) reaches a plateau after which further additions of our target material do not result in an improved electrochemical performance. This 'critical mass' of modification is likely due to the structure of the 2D MoS_2 nanosheet altering to that of a bulk formation (see earlier), thereby exposing less edge sites and thus inhibiting the beneficial electrochemical properties of single-, few-, quasi- MoS_2 nanosheets. Alternatively, this plateau could signify the mass (a critical mass of *ca*. 1009 ng cm^{-2} of the 2D MoS_2 nanosheets) at which the structure of MoS_2 can no longer structurally support itself upon the electrode surface (becoming unstable) diminishing and detaching from the surface of the electrode, eliminating the catalytic advantages of further additions (such that in some cases the catalytic response begins to deteriorate). Similar observations have been reported for the case of graphene.[79-82] This could arise due to the disconnection of 2D MoS_2 nanosheet layers during the course of the experiment (*i.e.* instability of the modified layer on the electrode surface due to the large quantity/mass present) which is bought about once such a 'critical mass' is achieved.

The intra-repeatability of the modified and unmodified SPEs were tested ($N = 3$). The % Relative Standard Deviation (% RSD) in the onset potential of the HER was found to be *ca*. 0.8, 1.4, 1.5, and 4.6 % at the 0 (unmodified), 252, 1009 and 2019 ng cm^{-2} modified SPEs respectively. It is clear that the % RSD increases with greater modifications of the MoS_2, likely a result of the factors stated above and potentially resulting in the reduced catalytic effects. Furthermore, the % RSD in the current densities observed were found to be *ca*. 12.4, 13.5, 10.5, and 15.5 % at the 0 (unmodified), 252, 1009 and 1771 ng cm^{-2} modified SPEs respectively. The high RSD values in this case are indicative of the structural instability of the deposited 2D MoS_2 nanosheet film on the underlying electrode surface, which likely leads to delamination and thus high levels of variation within the effective surface area and currents passed.

From the above inferences, we suggest that the structural model of 2D MoS_2 nanosheets is likely that of re-assembly, such that upon modification with increasing amounts of 2D MoS_2 nanosheets, bulk layers of MoS_2 materialise upon the surface of our support electrodes.[79, 81]

Electrochemical impedance spectroscopy (EIS) was used to determine the impedance of the electrode system as coverage of 2D MoS_2 nanosheets was increased, see ESI Figure. 10.[70] It was observed that the charge transfer resistance (Ω) for all electrodes decreased after modification with 252 ng cm^{-2} 2D MoS_2 nanosheets and further decreased after modification with 1009.5 ng cm^{-2}. Again a plateauing was observed in the response with increased coverage (for example after modification with 2019 ng cm^{-2}). The Ω values of the unmodified SPE (3.51×10^5 Ω) reduced to 1.69×10^5 Ω after 252 ng cm^{-2} and then to 3.27×10^3 Ω upon a 1009 ng cm^{-2} 2D MoS_2 nanosheet modification, after which the response plateaued, having an impedance value of 3.21×10^3 Ω by modification with 2019 ng cm^{-2}. Error values for the aforementioned results were recorded as 1.78×10^{-4}, 1.73×10^{-3}, 1.2×10^{-2}, and 1.21×10^{-2} Ω respectively. This EIS supports the above inferences and indicates that the 2D MoS_2 is an effective electrocatalyst with respect to the HER when deposited on a carbon electrode surface.

Finally, it is essential to assess the electrochemical stability of 2D MoS_2 nanosheets as a catalyst for the HER when drop coated onto an electrode surface (following on from the reported % RSD values noted above). This is a practical consideration for real applications where durability and longevity are necessary.[2, 27, 68] SPEs were used as a representative example for the four carbon based electrodes used within this study. A 1000 cycle voltammetry scan from 0 to –0.8 V at 25 mVs^{-1} was performed on SPEs modified with 252, 1009, 2019 ng cm^{-2} of 2D MoS_2 nanosheets. A decrease in the catalytic activity of each electrode was observed (see Figure. 9). At 0.6 V the decrease from the initial scan current was 6.8%, 32.3%, 26.9% for the SPEs modified with 252, 1009 and 2019 ng cm^{-2} respectively. The observed activity loss is significant especially for the 1009 and 2019 ng cm^{-2} modified electrodes. According to Shin, *et al*. [68] high stability of amorphous MoS_2 is rarely reported with the decrease in activity being associated with either: surface absorbatives which may poison the active sites of the 2D MoS2 nanosheets; [47] or the delamination of the 2D MoS2 nanosheets from the substrate. [47] However, it is likely a combination of these two effects with the delamination of 2D MoS_2 nanosheets becoming more prevalent at higher modifications. This inference is supported by the EIS observations detailed earlier. Another consideration in terms of industrial application is cost of the four carbon based electrodes studied, the GC offered the greatest current density and most noted HER onset potential decrease upon modification with 2D MoS_2 nanosheets. GC's production cost makes its application as a catalyst on an industrial scale economically unfeasible. The SPE offers an attractive alternative to using GC in real-world industrial applications. After modification with 2D MoS_2 nanosheets, the HER onset potential is lowered to a value equivalent of GC's. One issue could potentially be that the modified SPE exhibits a lower current density compared to that of GC, however, due to the nature of SPE's production they have can be produced to a wide manner of tailorability, varying in shape, surface area and carbon composition. As such SPEs can be produced with a larger surface area than that of GC, thereby increasing the currents possible and ultimately the amount of hydrogen produced. This combined with the ultra-low cost of fabricating SPEs makes them an exceptionally cost effective and easily producible supporting electrode material for HER. There is potential to incorporate 2D MoS_2 nanosheets into the carbon based inks used to produce SPEs, thereby eliminating the time consuming modification step. Further research aimed at identifying and resolving the reason for the poor catalytic stability is essential if 2D MoS_2 nanosheet modified SPEs have a future industrial application.

4. Conclusions

We have explored the catalytic performance of 2D MoS_2 nanosheets towards the HER. In order to overcome issues prevalent within the literature and to enable us to ascertain the true electrochemical performance of our commercially sourced MoS_2 we modified a range of carbon based underlying support electrodes, namely GC, BDD, EPPG and SPEs; this approach is usually neglected within the literature; Application of the MoS_2 modified electrodes revealed a catalytic performance towards the HER, with lower onset potentials and higher current densities observed when utilising our target material; the supporting electrode was found to be of key importance, influencing the improvements observed in the electrochemical performance. This indicates that 2D MoS_2 nanosheet modified electrodes can potentially serve as a viable, low cost and more abundant replacement to current Pt based electro-catalysts.

This work is distinct from the literature given that we have also correlated our electrochemical responses with supplementary Raman mapping of the electrode surface (and other complementary physicochemical characterisation) whilst exploring the effect of MoS_2 coverage. Coverage studies revealed that the catalytic effect of the 2D MoS_2 nanosheets increased (as indicated by ToF and 'number of active sites' calculations) until a 'critical mass' (coverage) was achieved, after which the response was observed to plateau. The likely cause of this effect is inferred herein and has clear implications (in this case and) when employing other 2D nanosheet modified electrodes within the literature.

We have provided insights into the observable electrochemistry and HER mechanism prevalent at 2D MoS_2 nanosheet modified electrodes, which has clear potential to be beneficially applied/utilised as an electrocatalyst if the diligent control measures reported herein are sufficiently applied.

Table 1. Comparison of current literature reporting the use of MoS$_2$ as a catalyst explored towards the HER.

Catalyst	Electrode / supporting material	Loading (μg cm^{-2})	Electrolyte	HER onset (–mV)	Tafel (mV dec^{-1})	Reference
MoS$_2$	Silver	–	0.5 M H_2SO_4	~ -0.15	*55-60*	83
MoS$_2$	CP	4	0.5 M H_2SO_4	-200	*120*	69
Narrow sheet MoS$_2$	GC	280	0.5 M H_2SO_4	-103	*49*	45
MoS$_2$/ CoSe$_2$	GC	~280	0.5 M H_2SO_4	11	*36*	84
MoS$_2$/ MCN	GC	190	0.5 M H_2SO_4	-100	*41*	85
MoS$_2$/RGO	GC	285	0.5 M H_2SO_4	-100	*41*	27
MoSx	GC	9	1 M H_2SO_4	–	*40*	13
MoS$_3$	GC	32	1 M H_2SO_4	~ -100	*54*	86
Fe- MoS$_2$	GC	30.4	1 M H_2SO_4	–	*39*	87
MoS$_2$ nanosheets	GC	48	0.5 M H_2SO_4	~ -150 to -200	*70*	32
2D MoS$_2$	GC	280 ❖	0.5 M H_2SO_4	-93	*42*	88
MoS$_2$	GC	~8.5	0.5 M H_2SO_4	–	*86*	72
MoS$_2$ film	GC	–	0.5 M H_2SO_4	–	*ca 140*	46
Defect rich MoS$_2$ nanosheets	GC	285	0.5 M H_2SO_4	-120	*50*	77
MoS$_2$ nanosheets	GC	–	0.5 M H_2SO_4	~ -100	*ca 40*	43
Amorphous MoS$_X$ films	GC	–	1 M H_2SO_4	–	*40*	28
MoS$_2$ NAS	GC	–	0.5 M H_2SO_4	-54	*100*	26
Annealed MoS$_2$/Ag	Ag/PET	6	0.5 M H_2SO_4	–	*154*	33
MoS$_2$/Ag Strain 0% *	Ag/PET	6	0.5 M H_2SO_4	–	*145*	33
MoS$_2$/Ag Strain *0.005%* *	Ag/PET	6	0.5 M H_2SO_4	–	*141*	33
MoS$_2$/Ag strain *0.01%* *	Ag/PET	6	0.5 M H_2SO_4	–	*138*	33
MoS$_2$/Ag strain *0.02%* *	Ag/PET	6	0.5 M H_2SO_4	–	*135*	33
MoS$_2$/Ag	Ag/PET	2	0.5 M H_2SO_4	–	*152*	33
MoS$_2$/Ag strain *0.01%* *	Ag/PET	2	0.5 M H_2SO_4	–	*142*	33
MoS$_2$/Ag	Ag/PET	6	0.5 M H_2SO_4	–	*142*	33
MoS$_2$/Ag strain *0.01%* *	Ag/PET	6	0.5 M H_2SO_4	–	*138*	33
MoS$_2$/Ag	Ag/PET	12	0.5 M H_2SO_4	–	*143*	33
MoS$_2$/Ag strain *0.01%* *	Ag/PET	12	0.5 M H_2SO_4	–	*140*	33
MoS$_2$ nanoparticles	Graphite	–	–	-100 to -200	–	7
Ni-Mo nanopowder	Ti	1	2 M KOH	-70	–	89
Ni-Mo nanopowder	Ti	3	0.5 M H_2SO_4	-80	–	89
Ni-Mo nanopowder	Ti	13.4	2 M KOH	-100	–	89

Amorphous MoSx	GC	(10^{17} sites cm^{-2})	0.5 M H_2SO_4	-200	60	47
2D MoS_2 nanosheets	GC	1.019	0.5 M H_2SO_4	~ -480	40	This work
2D MoS_2 nanosheets	EPPG	1.267	0.5 M H_2SO_4	~ *-450*	74	This work
2D MoS_2 nanosheets	BDD	1.267	0.5 M H_2SO_4	~ *-450*	90.9	This work
2D MoS_2 nanosheets	SPE	1.267	0.5 M H_2SO_4	~ *-440*	92	This work

Key; **–:** Value unknown; **GC:** glassy carbon; **CP**: carbon paper; **MCN:** mesoporous carbon nanospheres; **RGO**: reduced graphene oxide; **❖:**Optimised Loading; **NAS:** nano-assembled structures; **PET:** polyethylene terephthalate; **EPPG:** edge plane pyrolytic graphite; **BDD:** boron doped diamond; **SPE:** screen-printed graphite electrode; ***:** mechanical bent tensile-strain-induced two dimensional MoS_2 nanosheets

Table 2. The determined roughness factor (R_F) values and the number of active sites (per cm^2) for BDD, EPPG, GC and SPE all of which had been modified with 0, 252, 1009, 2019 ng cm^{-2} 2D MoS$_2$ nanosheets. Values determined using double layer capacitance obtained *via* cyclic voltammetry between the potential range of 0.01V and 0.1V.

Electrode	MoS$_2$ Modification (ng cm^{-2})	Roughness Factor	Number of active sites
BDD	2019	2.2	2.01 x10^{12}
	1009	1.5	1.38 x10^{11}
	252	0.3	3.03 x10^{11}
EPPG	2019	7.7	7.05 x10^{12}
	1009	5.5	5.05 x10^{12}
	252	4.2	3.84 x10^{12}
GC	2019	2.6	2.35 x10^{12}
	1009	2.1	1.95 x10^{12}
	252	1.0	8.95 x10^{11}
SPE	2019	4.8	4.43 x10^{12}
	1009	3.3	3.00 x10^{12}
	252	1.0	9.36 x10^{11}

Figure. 1 Raman spectra of the commercially sourced 2D MoS_2 nanosheets immobilised upon a silicon wafer.

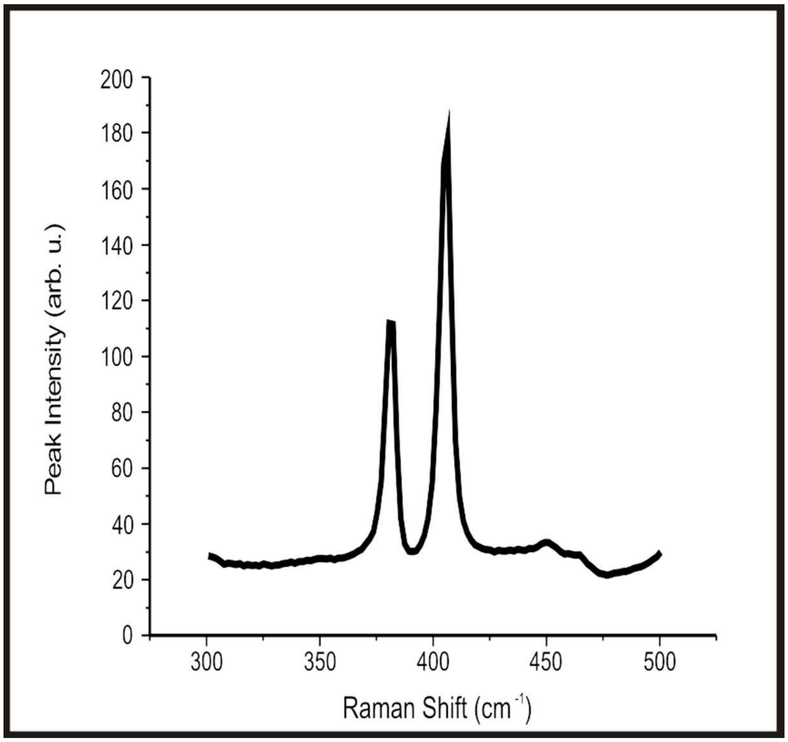

Figure. 2 Typical cyclic voltammetric response of 2D MoS_2 nanosheets immobilised upon a SPE in pH 7 phosphate buffer solution (PBS). First scan: solid black line. Second scan (representative of subsequent scans): red dotted line. Scan rate: 5 mVs^{-1} (*vs.* SCE).

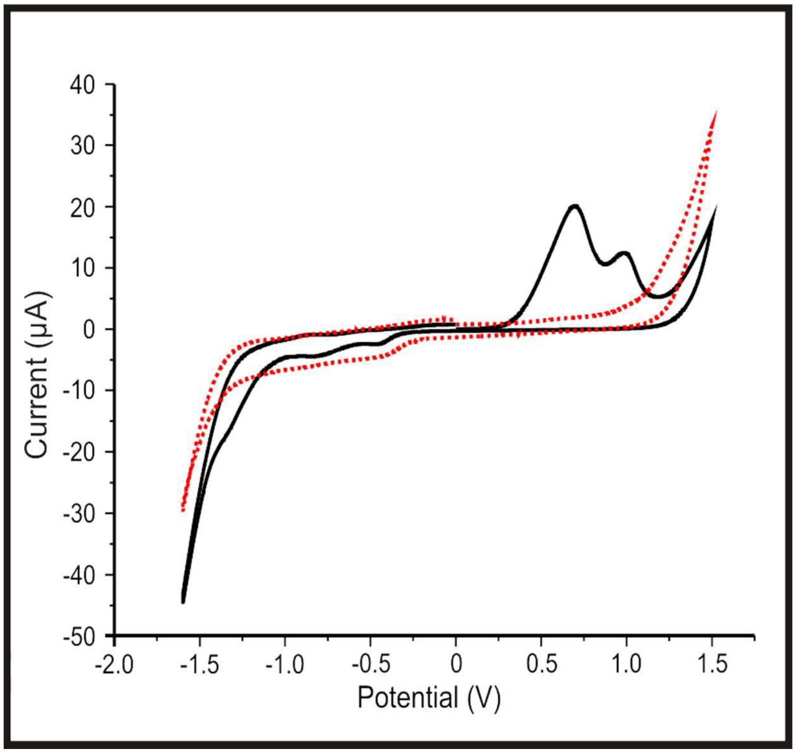

Figure. 3 (A) Linear sweep voltammetry (LSV) of unmodified EPPG, GC, SPE, BDD and Pt electrodes showing the onset of the HER. In all cases, scan rate: 25 mVs^{-1} (*vs.* SCE). Solution composition: 0.5 M H_2SO_4. (B) Tafel analysis; potential *vs.* natural log (ln) of current density for faradaic section of the LSV presented in (A).

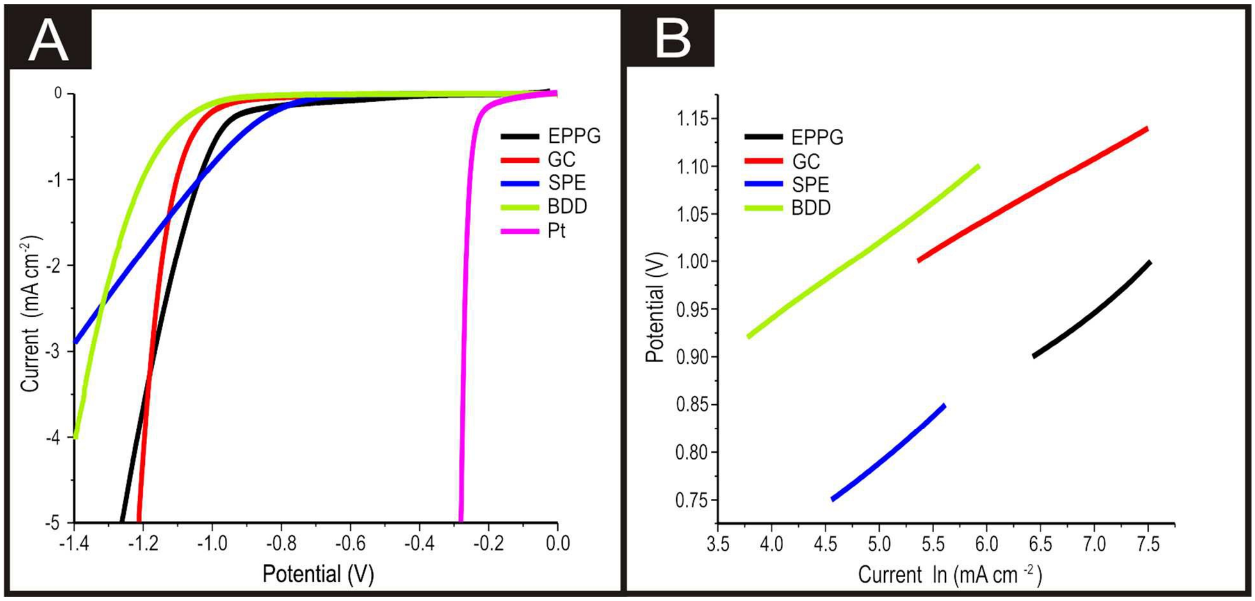

Figure. 4 (A) LSV of 1267 ng cm^{-2} modified EPPG, GC, SPE, BDD electrodes and an unmodified Pt electrode showing the onset of the HER. In all cases, scan rate: 25 mVs^{-1} (*vs.* SCE). Solution composition: 0.5 M H_2SO_4. (B) Tafel analysis; potential *vs.* natural log (ln) of current density for Faradaic section of the LSV presented in (A).

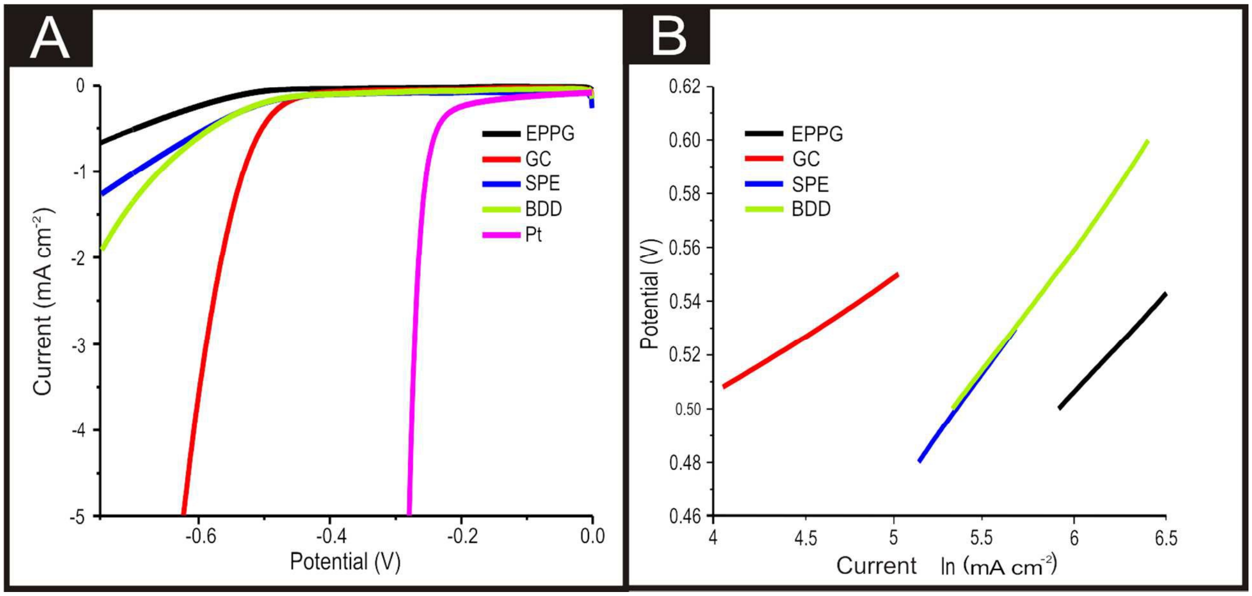

Figure. 5 (A) Raman Spectra peak intensity and position for 504 (black), 1009 (red), 2019 (blue) and 2533 (green) ng cm^{-2} 2D MoS$_2$ nanosheet modifications on SPEs. (B) Depicts 2D MoS$_2$ nanosheet coverage plotted against Raman peak intensity for E_{2g}^1 (black) and A$_{1g}$ (red) vibrational bands, showing a constant peak distance of 24.7 cm^{-1} at all coverages.

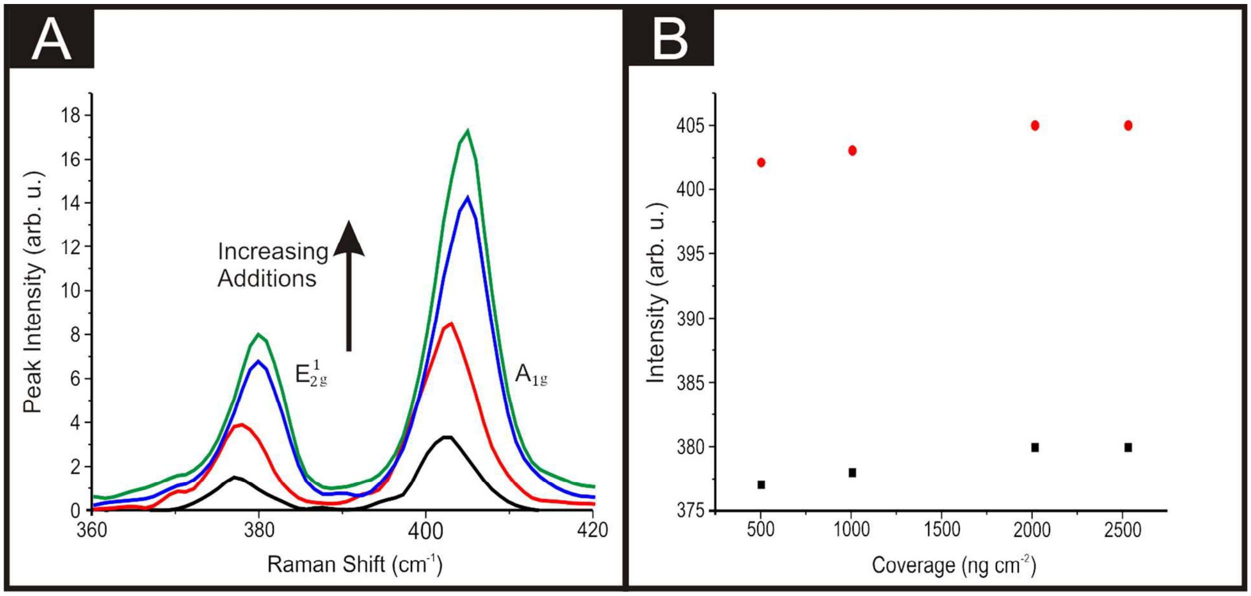

Figure 6. Raman maps representing various MoS_2 coverages onto an underlying SPE. Coverages of 2D MoS_2 nanosheets: 0 (A), 504 (B), 1009 (C), 2019 (D), and 2533 (E) ng cm^{-2}. Raman intensities recorded at 405 cm^{-1}.

(See additional document entitled " Figure 6" for Figure 6)

Figure. 7 Raman maps of SPE surface, each point showing the intensity ratio between the sum of the characteristic MoS_2 peak areas (380 and 405 cm^{-1}) against the area of the underlying graphite peak (1550 cm^{-1}). Using varying surface coverages of our 2D MoS_2 nanosheets; 504 (A), 1009 (B), 2019 (C) and 2533 (D) ng cm^{-2}. The grey maps are the modified electrodes and the black map in each represents an unmodified electrode surface.

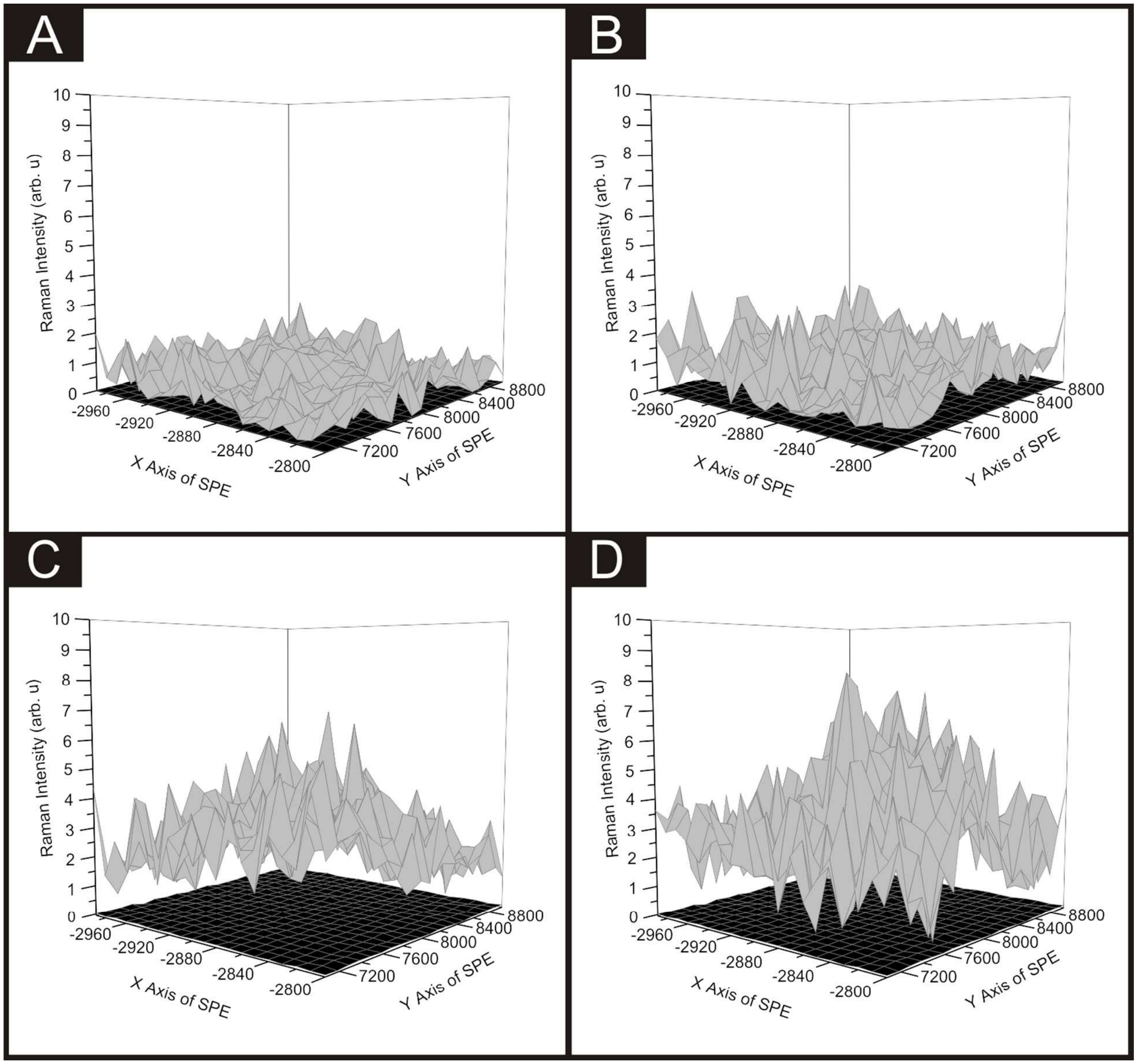

Figure. 8 Current density values taken at –0.75 V from linear sweep voltammetry from 0, 128.6, 252, 504, 762. 1009, 1267, 1524 and 1771 ng cm^{-2} 2D MoS_2 nanosheets immobilised upon: (A) EPPG, (B) GC, (C) SPE (D) BDD. Each graph showing the plateauing effect of current density when a critical mass of the 2D MoS_2 nanosheets is deposited onto the electrodes surface. Error bars are the average and standard deviation of 3 replicates.

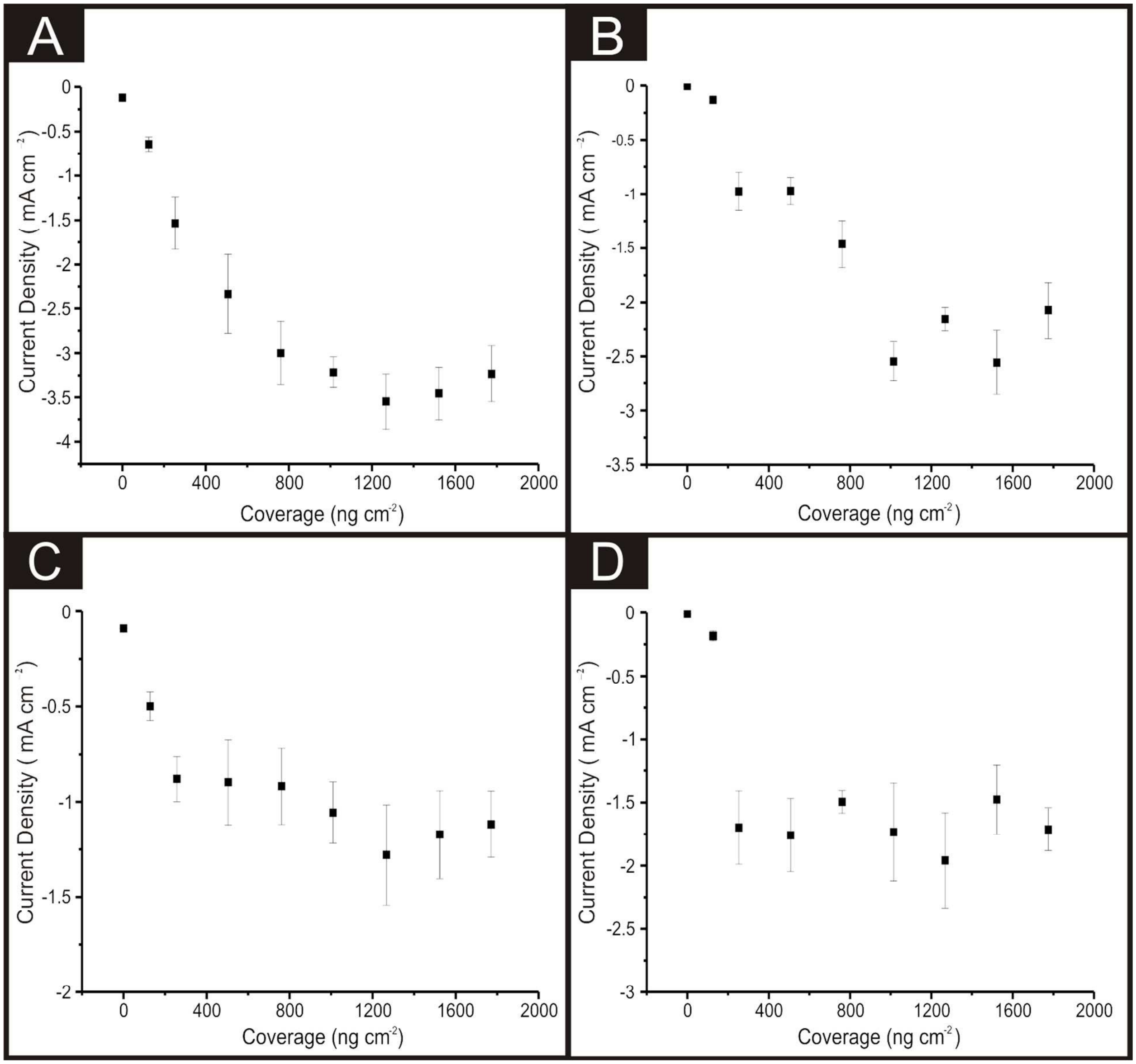

Figure. 9 Stability studies using SPEs modified with (A) 252, (B) 1009 and (C) 2019 ng cm^{-2} 2D MoS$_2$ nanosheets. Cyclic Voltammetry was performed between the potential range of 0 to –0.8 V, repeated for 1000 cycles, these figures show the initial (black line) and 1000th (red line) scans.

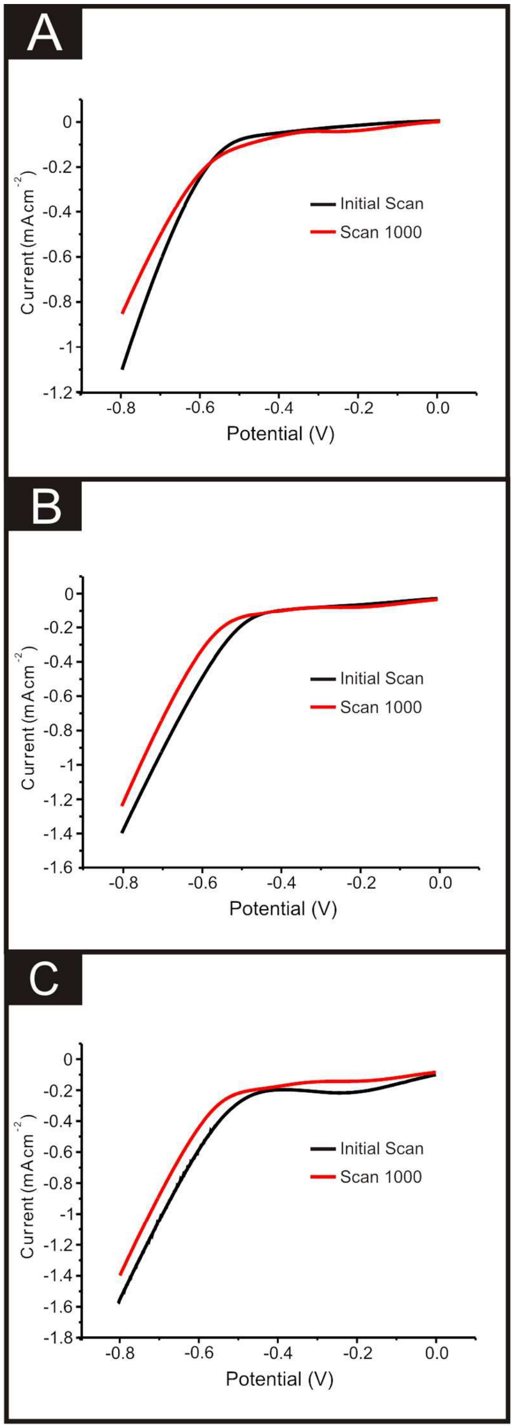

Electronic Supporting Information

ESI Figure. 1 Extinction spectra for the commercially sourced MoS_2 nanosheets dispersed in ethanol (9 mg L^{-1}).

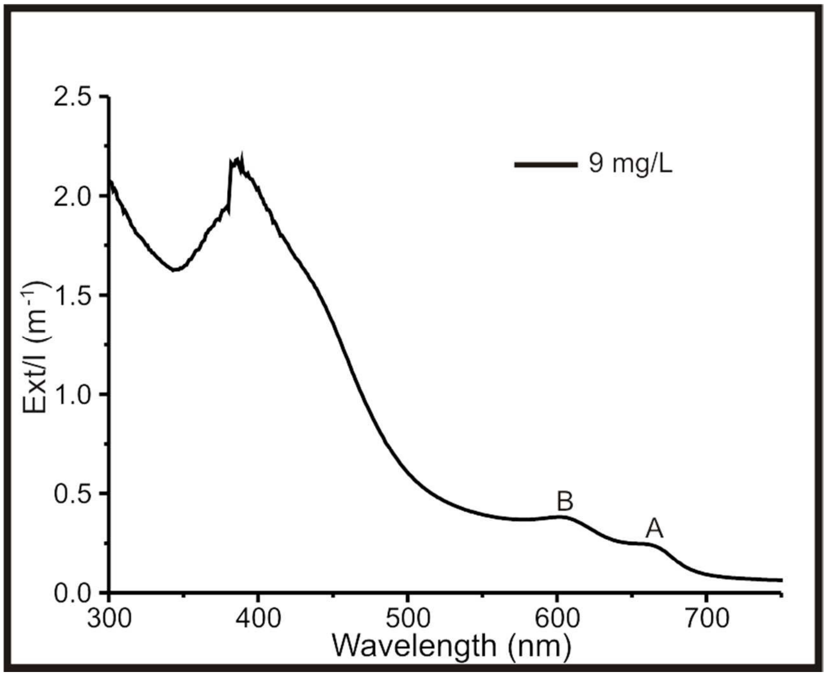

ESI Figure. 2 (A) SEM image of a multi-layered 2D MoS_2 nanosheet flake on top of few layer 2D MoS_2 nanosheets immobilised on a silicon wafer along with EDS analysis highlighting the underlying silicon support (B, in red), molybdenum (C, in green) and sulphur (D, in blue) coverage of image A respectively.

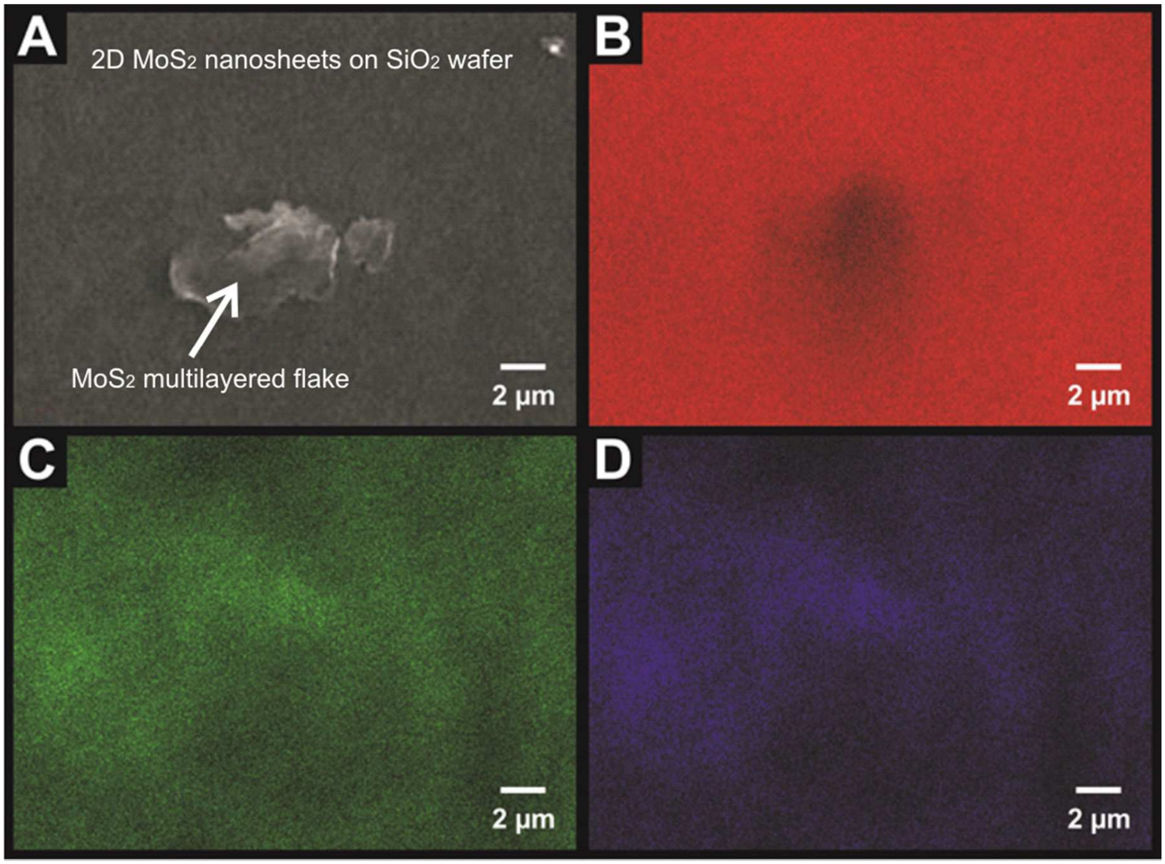

ESI Figure. 3 TEM images of the commercially sourced 2D MoS_2 nanosheets deposited onto a holey carbon grid. (A) TEM image at 5,800 times magnification (scale bar: 2 μm), (B) TEM image at 13,500 times magnification (scale bar: 1 μm).

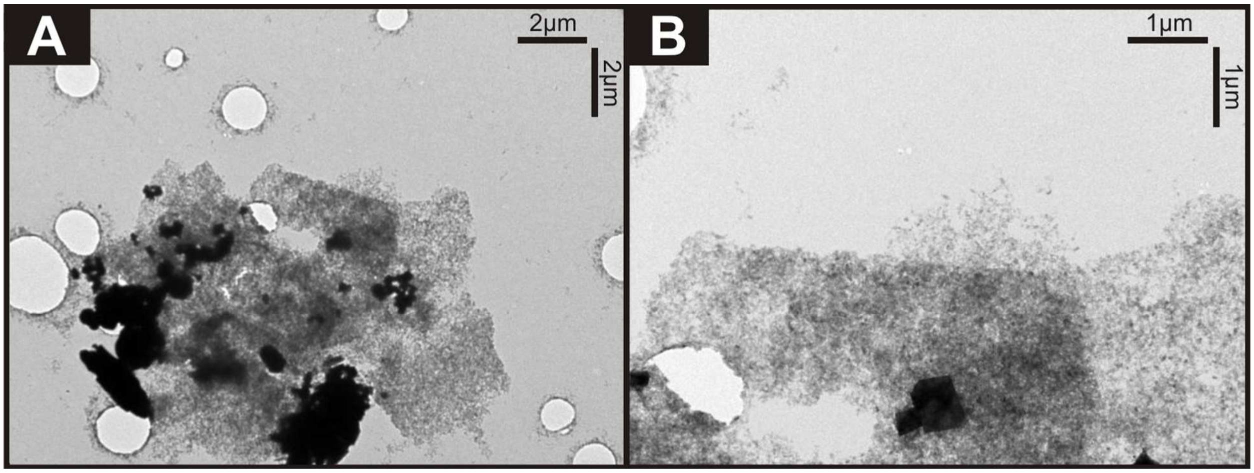

ESI Figure. 4 XRD spectra of the 2D MoS_2 nanosheets deposited onto a glass slide between 10 and 100 2θ, showing a characteristic peak at 14 2θ.

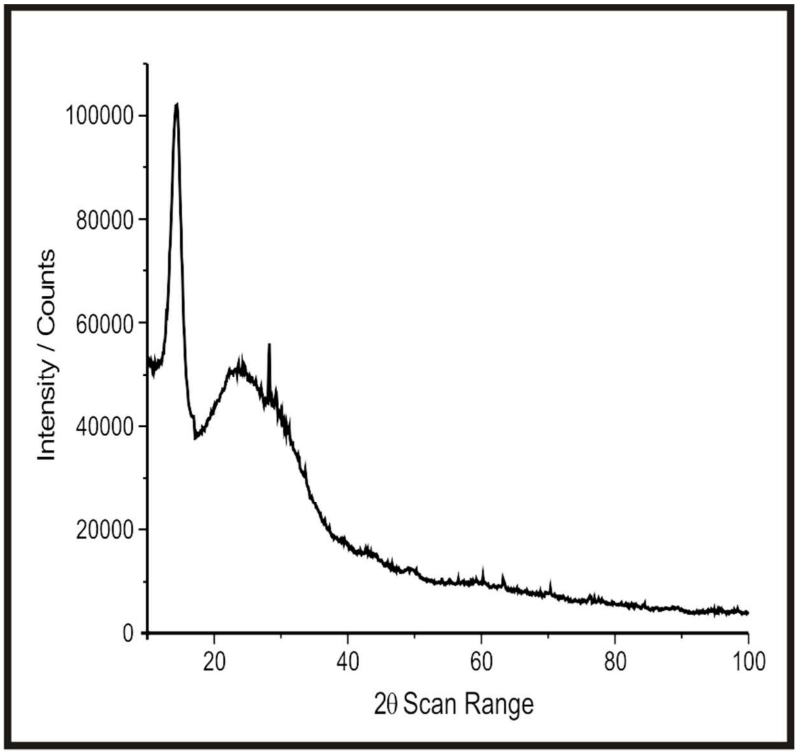

ESI Figure. 5 XPS survey spectrum for a sample of the 2D MoS_2 nanosheets once deposited onto a Si (111) wafer showing a 1:2.2 concentration percentage for Mo and S respectively.

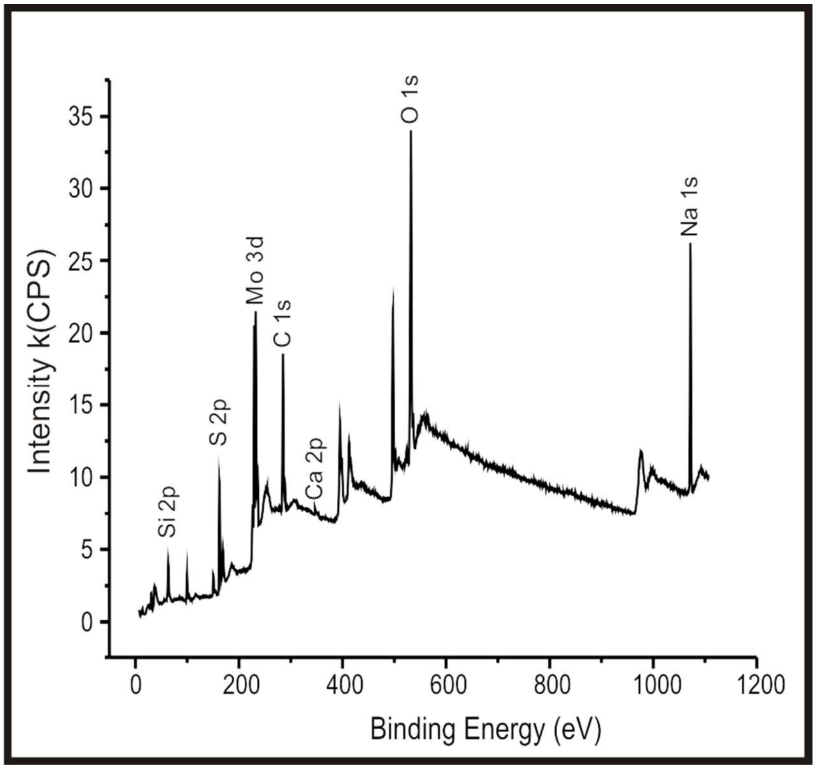

ESI Figure. 6 Curve fitted XPS Mo 3d spectrum

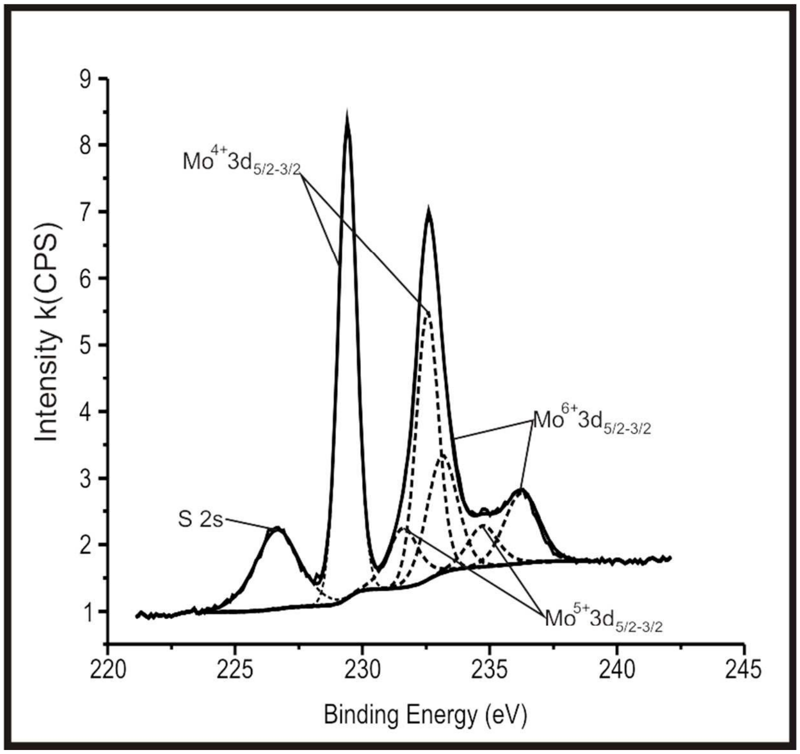

ESI Table 1. Compositional analysis of XPS spectra presented in ESI figure 5, shown in atom percentage concentration, excluding H which is not detected by this technique.

Element	**Atom % Concentration**
Na 1s	8.36
Mo 3d	7.44
C 1s	34.41
Ca 2p	0.61
S 2p	16.3
Si 2p	5.47
O 1s	27.4

Roughness Factor Calculations

Method 1

In order to use the ToF formula described by Benck, *et al.* [47] it was essential for roughness factors of the three modified SPE surfaces to be calculated. These were calculated using a ZeGage 3D Optical Surface Profiler, produced by Zygo. The surface topography of the 2D MoS_2 nanosheets was measured once deposited onto the SPEs, and these measurements were subsequently used to provide a value for the roughness factor (R_F) used in this work. The surface profile maps are shown in ESI Figure 7 were analysed using a Matlab script based on the following equation:

$$R_F = \frac{\sum_{k=0}^{M-2} \sum_{i=0}^{N-2} A_{kl}}{(M-1)(N-1)\delta x \delta y} \qquad [1]$$

where M and N are the total number of points in the x and y directions respectively, x and y are the distances between the points in the x and y directions, and where:

$$A_{kl} = \frac{1}{4}\left(\sqrt{\delta y^2 + \left(z(x_k,y_i) - z(x_k,y_{i+1})\right)^2} + \sqrt{\delta y^2 + \left(z(x_{k+1},y_i) - z(x_{k+1},y_{i+1})\right)^2}\right) + \left(\sqrt{\delta x^2 + (z(x_k,y_i) - z(x_{k+1},y_i))^2} + \sqrt{\delta y^2 + (z(x_k,y_{i+1}) - z(x_{k+1},y_{i+1}))^2}\right) \qquad [2]$$

with z being the height above the surface at a coordinate (x,y). Although similar to the surface area ratio (S_{dr}) typically used for surface topology measurements,[90] the equation has been modified to provide the ratio of interfacial area to the area of the projected horizontal plane, rather than the increment of the interfacial surface area to the projected horizontal plane. This modification has been made as the roughness factor is described as the ratio of the catalyst active surface area to the substrate geometric surface area.[47] The roughness factors were consistently found to occur in the range 1.918 to 1.934 even for the three SPEs modified with 252, 1009 and 2019 ng $cm^{-2}$of 2D MoS_2 nanosheets respectively. Clearly this shows that the WLP probes only the outside/upper layer of the exposed 2D nanosheets and is insensitive to the surface coverage/mass of material immobilised and does not provide us with the *electrochemically active area*. Clearly this approach will limited the interpretation of the ToF (see main text).

Method 2

Following the method of Shin *et al.* [68] the double layer capacitance can be used to calculate the active surface area of the 2D MoS_2 nanosheet modified SPE electrode. Using an unmodified SPE and SPEs modified with 0, 252, 1009 and 2019 ng cm^{-2} 2D MoS_2 nanosheets, cyclic voltammetry was performed using a potential range of 0.01 to 0.011 V, which is in the non-Faradaic window, at each of the following scan rates (20, 40, 60, 80, 100 mVs^{-1}). The potential range used is presumed to have no Faradaic processes occurring, therefore cathodic and anodic current densities are associated with charging of the electrical double layer (see ESI Figure. 8). ESI Figure. 9 shows the difference between the anodic and cathodic current at 0.06 V *versus* the corresponding scan rate. The slope of each set of points in ESI Figure. 9 being proportional to a doubling of the double layer capacitance. The double layer capacitance values determined are 8.7, 68, 218, 322 μF cm^{-2} for SPEs modified with 0, 252, 1009 and 2019 ng cm^{-2} 2D MoS_2 nanosheets respectively. The 7.8× increase in double layer capacitance from unmodified to 252 ng cm^{-2} 2D MoS_2 nanosheet modification reveals that post modification there is a significant adherence of 2D MoS_2 nanosheets upon the SPE electrode surface. There is a further 3.2× and 4.7× increase in the capacitance value from that of 252 to 1009 and 2019 ng cm^{-2} 2D MoS_2 nanosheets modifications respectively. It is inferred that this is associated with a thickening of the 2D MoS_2 nanosheets deposited. The disparity between the increase in capacitance and the increase in ng cm^{-2} 2D MoS_2 nanosheets is of interest and further study on the matter is required.

ESI Figure. 7 White light profilometry surface topography maps of SPE’s modified with (A) 252, (B) 1009 and (C) 2019 ng cm^{-2} of 2D MoS_2 nanosheets. It is evident that the surface roughness remains relatively constant with the increasing 2D MoS_2 nanosheet modification.

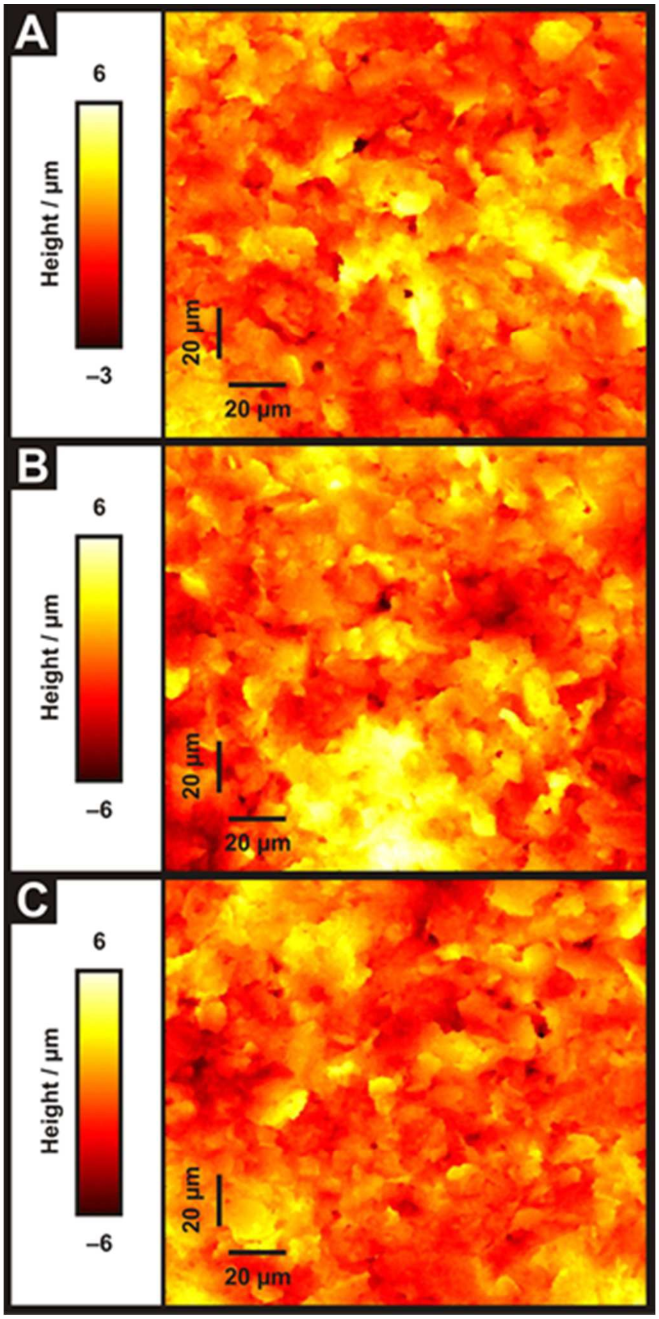

ESI Figure. 8

Cyclic voltammograms recorded in 0.5M H_2SO_4 solution for SPE's with varying amounts of 2D MoS_2 nanosheet modification; (A) 0, (B) 252, (C) 1009, (D) 2019 ng cm^{-2}.

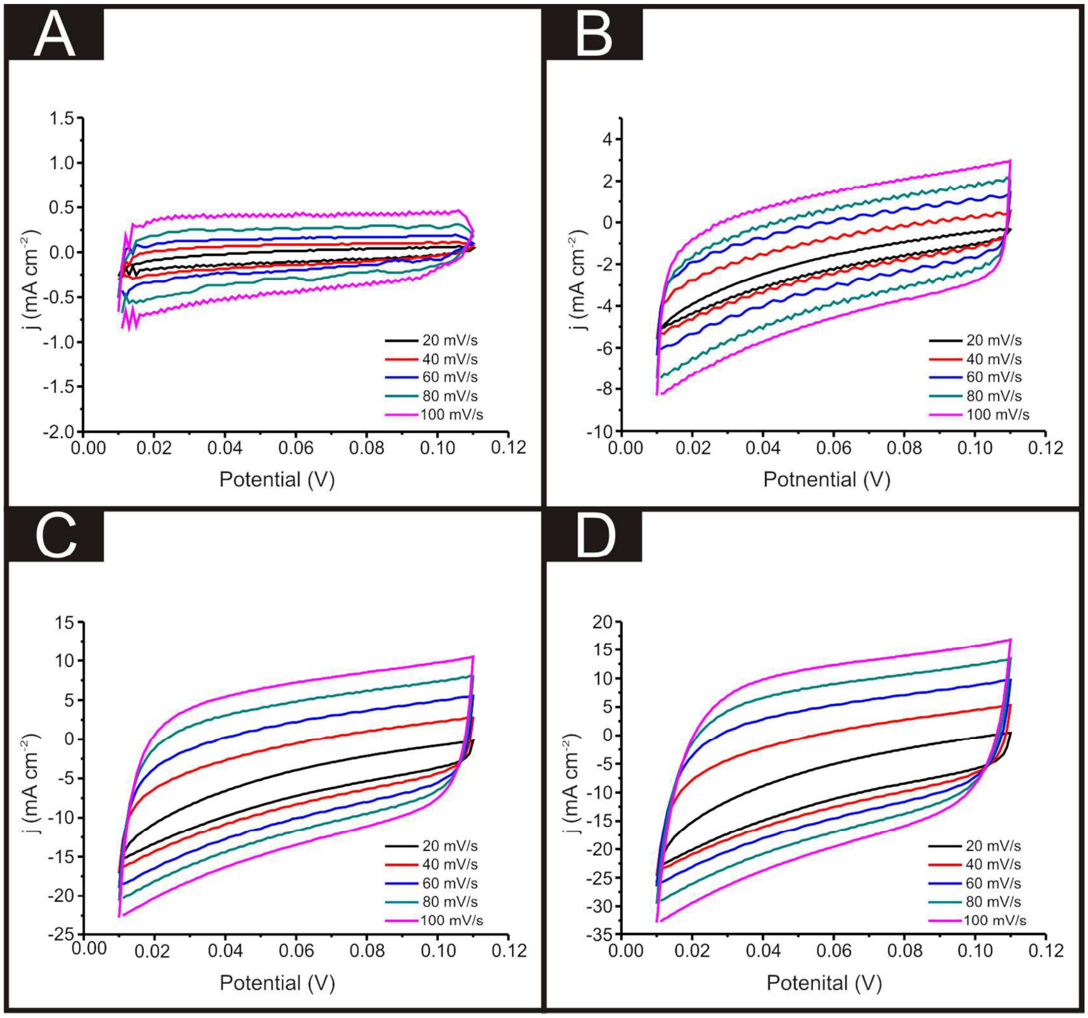

ESI Figure. 9 The difference in anodic and cathodic current density taken at +0.06 V *versus* scan rate (mVs^{-1} *vs.* SCE). The slope of the linear regression indicates the value of double layer capacitance (C_{dl}).

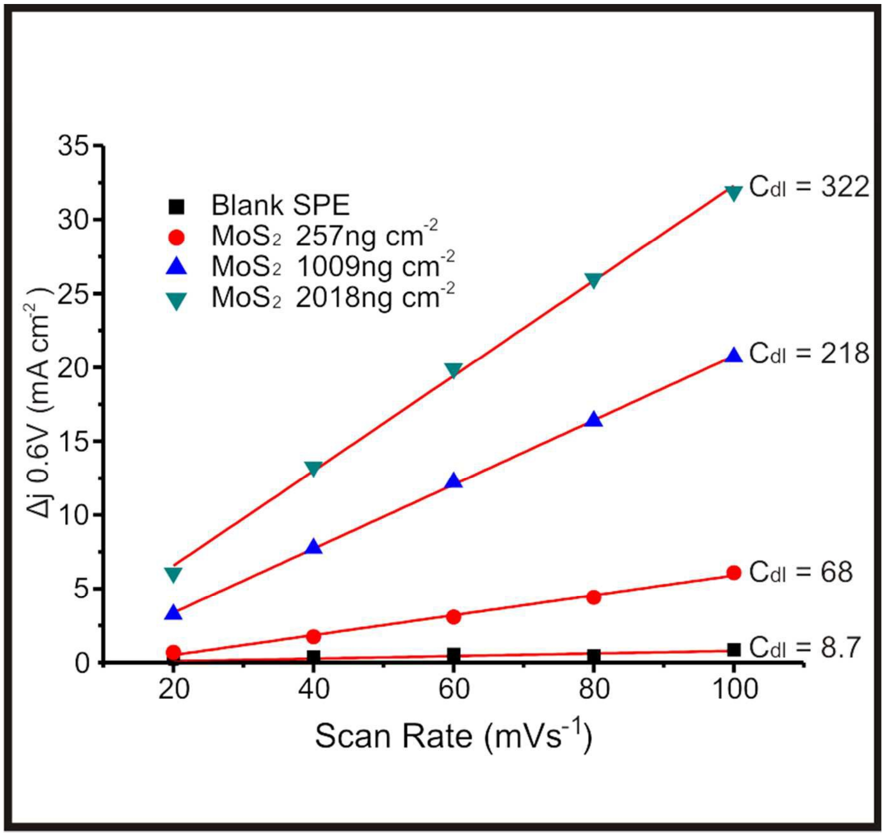

ESI Figure. 10 An electrochemical impedance spectroscopy (EIS) study showing charge transfer resistance (ohm) values for EPPG, GC, SPE and BDD against 2D MoS_2 nanosheet coverages' of 0, 252, 1009 and 2019 ng cm^{-2}. Increasing coverage leading to a decrease in EIS followed by a plateau. The EIS study was carried out in 0.5 M H_2SO_4, the frequency was from 0.1–100,000 Hz, and an amplitude of 10 mV (*vs*. SCE).

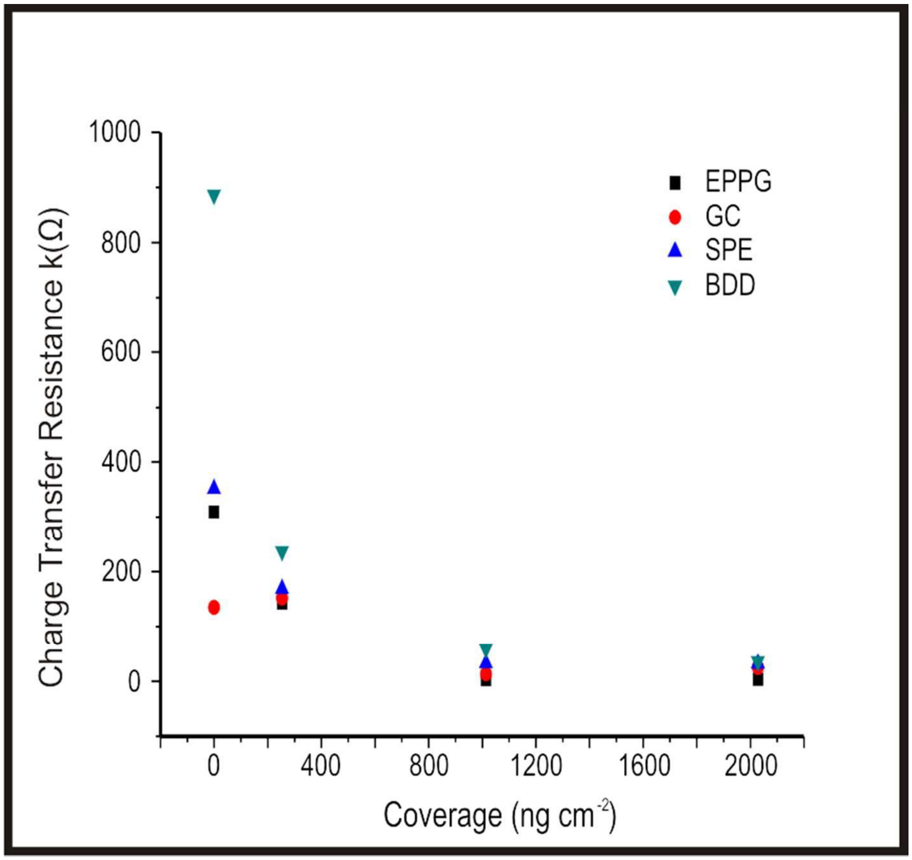

References

1. Y. Z. Yufei Zhao, Zhiyu Yang, Yiming Yan and Kening Sun, *Sci. Technol. Adv. Mater* 2013, 14.
2. T. Wang, L. Liu, Z. Zhu, P. Papakonstantinou, J. Hu, H. Liu and M. Li, *Energy Environ. Sci.*, 2013, 6, 625-633.
3. A. J. López-Menéndez, R. Pérez and B. Moreno, *J. Environ. Manage.*, 2014, 145, 368-373.
4. T. D. M. G. Schultz, G. P. Brasseur, W. Zittel, *Science* 2003, 302, 624-627.
5. T. Hua, R. Ahluwalia, L. Eudy, G. Singer, B. Jermer, N. Asselin-Miller, S. Wessel, T. Patterson and J. Marcinkoski, *J. Power Sources*, 2014, 269, 975-993.
6. J.Andrews and B.Shabani, *WIREs Energy Environ*, 2014, 3, 474-489.
7. B. Hinnemann, P. G. Moses, J. Bonde, K. P. Jørgensen, J. H. Nielsen, S. Horch, I. Chorkendorff and J. K. Nørskov, *J. Am. Chem. Soc.*, 2005, 127, 5308-5309.
8. M. Gratzel., *Inorg. Chem.*, 2005, 44, 6841-6851.
9. J. P. Barton and D. G. Infield, *IEEE Trans. Energy Convers*, 2004, 19, 441-448.
10. F. Blaabjerg, Z. Chen and S. B. Kjaer, *IEEE Trans. Power Electron.*, 2004, 19, 1184-1194.
11. N. M. Marković and P. N. Ross Jr, *Surf. Sci. Rep.*, 2002, 45, 117-229.
12. N. M. Marković, B. N. Grgur and P. N. Ross, *J. Phys. Chem. B*, 1997, 101, 5405-5413.
13. A. B. Laursen, S. Kegnaes, S. Dahl and I. Chorkendorff, *Energy Environ. Sci.*, 2012, 5, 5577-5591.
14. T. F. Jaramillo, K. P. Jørgensen, J. Bonde, J. H. Nielsen, S. Horch and I. Chorkendorff, *Science*, 2007, 317, 100-102.
15. B. X. Ya Yan , Zhichuan Xu , and Xin Wang *ACS Catal.*, 2014, 693‑1705.
16. K. Ravindra, L. Bencs and R. Van Grieken, *Sci. Total Environ.*, 2004, 318, 1-43.
17. R. L. McCreery, *Chem. Rev.*, 2008, 108, 2646-2687.
18. D. A. C. Brownson and C. E. Banks, *Electrochem. Commun.*, 2011, 13, 111-113.
19. M. Lu, K. E. Toghill and R. G. Compton, *Electroanalysis*, 2011, 23, 1089-1094.
20. M. Musameh, J. Wang, A. Merkoci and Y. Lin, *Electrochem. Commun.*, 2002, 4, 743-746.
21. A. Koca, *Int. J. Hydrogen Energy In*, 2009, 34, 2107-2112.
22. Y. Shen, J. Liu, J. Jiang, B. Liu and S. Dong, *J. Phys. Chem. B*, 2003, 107, 9744-9748.
23. J. Yin, J. B. Jia and L. D. Zhu, *In*, 2008, 33, 7444-7447.
24. Y. Zheng, Y. Jiao, Y. Zhu, L. H. Li, Y. Han, Y. Chen, A. Du, M. Jaroniec and S. Z. Qiao, *Nat Commun*, 2014, 5.
25. Z. Chen, D. Cummins, B. N. Reinecke, E. Clark, M. K. Sunkara and T. F. Jaramillo, *Nano Lett.*, 2011, 11, 4168-4175.
26. D. Y. Chung, S.-K. Park, Y.-H. Chung, S.-H. Yu, D.-H. Lim, N. Jung, H. C. Ham, H.-Y. Park, Y. Piao, S. J. Yoo and Y.-E. Sung, *Nanoscale*, 2014, 6, 2131‑2136.
27. Y. Li, H. Wang, L. Xie, Y. Liang, G. Hong and H. Dai, *J. Am. Chem. Soc.* , 2011, 133, 7296-7299.
28. D. Merki, S. Fierro, H. Vrubel and X. Hu, *Chem. Sci*, 2011, 2, 1262-1267.
29. Q. Liu, J. Tian, W. Cui, P. Jiang, N. Cheng, A. M. Asiri and X. Sun, *Angew. Chem.*, 2014, 126, 6828-6832.

30. L. F. Pan, Y. H. Li, S. Yang, P. F. Liu, M. Q. Yu and H. G. Yang, *Electrochem. Commun.*, 2014, 50, 13135-13137.
31. Y. H. Chang, C. T. Lin, T. Y. Chen, C. L. Hsu, Y. H. Lee, W. J. Zhang, K. H. Wei and L. J. Li, *Adv. Mater.*, 2013, 25, 756-760.
32. P. C. Joensen, E. D. Alberding, N. Frindt, R. F., *J. Phys. C: Solid State Phys.*, 1987, 20, 4043-4053.
33. J. H. Lee, W. S. Jang, S. W. Han and H. K. Baik, *Langmuir*, 2014, 30, 9866-9873.
34. S. Ji, Z. Yang, C. Zhang, Z. Liu, W. W. Tjiu, I. Y. Phang, Z. Zhang, J. Pan and T. Liu, *Electrochim. Acta*, 2013, 109, 269-275.
35. RadisavljevicB, RadenovicA, BrivioJ, GiacomettiV and KisA, *Nat Nano*, 2011, 6, 147-150.
36. S. Tongay, J. Zhou, C. Ataca, K. Lo, T. S. Matthews, J. Li, J. C. Grossman and J. Wu, *Nano Lett.*, 2012, 12, 5576-5580.
37. M.-L. Tsai, S.-H. Su, J.-K. Chang, D.-S. Tsai, C.-H. Chen, C.-I. Wu, L.-J. Li, L.-J. Chen and J.-H. He, *ACS Nano*, 2014, 8, 8317-8322.
38. C. Ataca, M. Topsakal, E. Aktürk and S. Ciraci, *J. Phys. Chem. C*, 2011, 115, 16354-16361.
39. N. A. Dhas and K. S. Suslick, *J. Am. Chem. Soc.*, 2005, 127, 2368-2369.
40. F. Cesano, S. Bertarione, A. Piovano, G. Agostini, M. M. Rahman, E. Groppo, F. Bonino, D. Scarano, C. Lamberti, S. Bordiga, L. Montanari, L. Bonoldi, R. Millini and A. Zecchina, *Catal. Sci. Technol.*, 2011, 1, 123-136.
41. S. S. Chou, M. De, J. Kim, S. Byun, C. Dykstra, J. Yu, J. Huang and V. P. Dravid, *J. Am. Chem. Soc.*, 2013, 135, 4584-4587.
42. D. Wang, Z. Pan, Z. Wu, Z. Wang and Z. Liu, *J. Power Sources*, 2014, 264, 229-234.
43. D. Voiry, M. Salehi, R. Silva, T. Fujita, M. Chen, T. Asefa, V. B. Shenoy, G. Eda and M. Chhowalla, *Nano Lett.*, 2013, 13, 6222-6227.
44. N. Tateishi, K. Yahikozawa, K. Nishimura and Y. Takasu, *Electrochim. Acta*, 1992, 37, 2427-2432.
45. M.-R. Gao, M. K. Y. Chan and Y. Sun, *Nat Commun*, 2015, 6.
46. Y. Yu, S.-Y. Huang, Y. Li, S. N. Steinmann, W. Yang and L. Cao, *Nano Lett.*, 2014, 14, 553-558.
47. J. D. Benck, Z. Chen, L. Y. Kuritzky, A. J. Forman and T. F. Jaramillo, *ACS Catal.*, 2012, 2, 1916-1923.
48. C. W. Foster, J. P. Metters and C. E. Banks, *Electroanalysis*, 2013, 25, 2275-2282.
49. A. B. Laursen, A. S. Varela, F. Dionigi, H. Fanchiu, C. Miller, O. L. Trinhammer, J. Rossmeisl and S. Dahl, *J. Chem. Educ.*, 2012, 89, 1595-1599.
50. D. Marin, F. Medicuti and C. Teijeiro, *J. Chem. Educ.*, 1994, 71, A277.
51. L. R. Cumba, J. P. Smith, D. A. C. Brownson, J. Iniesta, J. P. Metters, D. R. d. Carmo. and C. E. Banks, *Analyst*, 2015, 140, 1543-1550.
52. C. W. Foster, J. Pillay, J. P. Metters and C. E. Banks, *Sensors (Basel, Switzerland)*, 2014, 14, 21905-21922.
53. J. P. Metters, M. Gomez-Mingot, J. Iniesta, R. O. Kadara and C. E. Banks, *Sens. Actuators, B*, 2013, 177, 1043-1052.
54. E. P. Randviir, D. A. C. Brownson, J. P. Metters, R. O. Kadara and C. E. Banks, *PCCP*, 2014, 16, 4598-4611.
55. J. P. Smith, J. P. Metters, O. I. G. Khreit, O. B. Sutcliffe and C. E. Banks, *Anal. Chem.*,

2014, 86, 9985-9992.

56. O. Ramdani, J. P. Metters, L. C. S. Figueiredo-Filho, O. Fatibello-Filho and C. E. Banks, *Analyst*, 2013, 138, 1053-1059.
57. J. P. Smith, J. P. Metters, D. K. Kampouris, C. Lledo-Fernandez, O. B. Sutcliffe and C. E. Banks, *Analyst*, 2013, 138, 6185-6191.
58. Graphene Supermarket, https://graphene-supermarket.com/MoS2-Pristine-Flakes-in-Solution.html, [24/11/2014].
59. Innovation in Surface Spectroscopy and Microscopy Systems, http://www.specs.de/cms/front_content.php?idcat=209, Accessed 22/05/2015.
60. M. P. Seah and S. J. Spencer, *J. Electron. Spectrosc. Relat. Phenom.*, 2006, 151, 178-181.
61. J. H. Scofield, *J. Electron. Spectrosc. Relat. Phenom.*, 1976, 8, 129-137.
62. CasaXPS, http://www.casaxps.com/, Accessed 22/05/2015.
63. E. Varrla, C. Backes, K. R. Paton, A. Harvey, Z. Gholamvand, J. McCauley and J. N. Coleman, *Chem. Mater.*, 2015, 27, 1129-1139.
64. C. Backes, R. J. Smith, N. McEvoy, N. C. Berner, D. McCloskey, H. C. Nerl, A. O' Neill, P. J. King, T. Higgins, D. Hanlon, N. Scheuschner, J. Maultzsch, L. Houben, G. S. Duesberg, J. F. Donegan, V. Nicolosi and J. N. Coleman, *Nat Commun*, 2014, 5.
65. L. Yadgarov, C. L. Choi, A. Sedova, A. Cohen, R. Rosentsveig, O. Bar-Elli, D. Oron, H. Dai and R. Tenne, *ACS Nano*, 2014, 8, 3575-3583.
66. J. A. Wilson and A. D. Yoffe, *A. D. Adv. Phys.*, 1969, 19, 193-335.
67. H. Li, Q. Zhang, C. C. R. Yap, B. K. Tay, T. H. T. Edwin, A. Olivier and D. Baillargeat, *Adv. Funct. Mater.*, 2012, 22, 1385-1390.
68. S. Shin, Z. Jin, D. H. Kwon, R. Bose and Y.-S. Min, *Langmuir*, 2015, 31, 1196-1202.
69. J. Bonde, P. G. Moses, T. F. Jaramillo, J. K. Norskov and I. Chorkendorff, *Faraday Discuss.*, 2009, 140, 219-231.
70. S. Ding, D. Zhang, J. S. Chen and X. W. Lou, *Nanoscale*, 2012, 4, 95-98.
71. A. H. Loo, A. Bonanni, A. Ambrosi and M. Pumera, *Nanoscale*, 2014, 6, 11971-11975.
72. D. Kong, H. Wang, J. J. Cha, M. Pasta, K. J. Koski, J. Yao and Y. Cui, *Nano Lett.*, 2013, 13, 1341-1347.
73. C. Lee, H. Yan, L. E. Brus, T. F. Heinz, J. Hone and S. Ryu, *ACS Nano*, 2010, 4, 2695-2700.
74. K. Zhang, S. Hu, Y. Zhang, T. Zhang, X. Zhou, Y. Sun, T.-X. Li, H. J. Fan, G. Shen, X. Chen and N. Dai, *ACS Nano*, 2015, 9, 2704-2710.
75. J. D. Benck, T. R. Hellstern, J. Kibsgaard, P. Chakthranont and T. F. Jaramillo, *ACS Catal.*, 2014, 4, 3957-3971.
76. S. Helveg, J. V. Lauritsen, E. Lægsgaard, I. Stensgaard, J. K. Nørskov, B. S. Clausen, H. Topsøe and F. Besenbacher, *Physical Review Letters*, 2000, 84, 951-954.
77. J. Z. Xie, Hao. Li, Shuang. Wang, Ruoxing. Sun, Xu. Zhou, Min. Zhou, Jingfang. Lou, Xiong Wen. Xie, Yi, *Adv. Mater.*, 2013, 25, 5807-5813.
78. M. A. Lukowski, A. S. Daniel, F. Meng, A. Forticaux, L. Li and S. Jin, *J. Am. Chem. Soc.*, 2013, 135, 10274-10277.
79. D. A. C. Brownson, A. C. Lacombe, D. K. Kampouris and C. E. Banks, *Analyst*, 2012, 137, 420-423.
80. D. A. C. Brownson, L. C. S. Figueiredo-Filho, X. Ji, M. Gomez-Mingot, J. Iniesta, O. Fatibello-Filho, D. K. Kampouris and C. E. Banks, *J. Mater. Chem.A*, 2013, 1, 5962-5972.

81. D. A. C. Brownson, L. J. Munro, D. K. Kampouris and C. E. Banks, *RSC Adv.*, 2011, 1, 978-988.
82. D. A. C. Brownson, D. K. Kampouris and C. E. Banks., *Chem. Soc. Rev.*, 2012, 41, 6944-6976.
83. T. F. Jaramillo, K. P. Jørgensen, J. Bonde, J. H. Nielsen, S. Horch and I. Chorkendorff, *Science*, 2007, 317, 100-102.
84. M.-R. Gao, J.-Z. Liang, Y.-R. Zheng, Y.-F. Xu, J. Jiang, Q. Gao, J. Li and S.-H. Yu, *Nat Commun*, 2015, 6.
85. X. Bian, J. Zhu, L. Liao, M. D. Scanlon, P. Ge, C. Ji, H. H. Girault and B. Liu, *Electrochem. Commun.*, 2012, 22, 128-132.
86. H. Vrubel, D. Merki and X. Hu, *Energy Environ. Sci.*, 2012, 5, 6136-6144.
87. D. Merki, H. Vrubel, L. Rovelli, S. Fierro and X. Hu, *Chem. Sci.*, 2012, 3, 2515-2525.
88. H. Zhu, F. Lyu, M. Du, M. Zhang, Q. Wang, J. Yao and B. Guo, *ACS Appl. Mater. Interfaces*, 2014, 6, 22126-22137.
89. J. R. McKone, B. F. Sadtler, C. A. Werlang, N. S. Lewis and H. B. Gray, *ACS Catal.*, 2012, 3, 166-169.
90. T. Patois, B. Lakard, S. Monney, X. Roizard and P. Fievet, *Synth. Met.*, 2011, 161, 2498-2505.